Rheological properties of the lower crust and upper mantle beneath Baja California: a microstructural study of xenoliths from San Quintin

Thomas F. van der Werf

Master Thesis
May 2016

Faculty of Geosciences
Department of Earth Sciences
Utrecht University

Abstract

Baja California is an active transtensional rift zone, which links the San Andreas Fault with the East Pacific Rise. The erupted basalts of the Holocene San Quintin volcanic field contain xenoliths, which sample the lower crust and upper mantle beneath Baja California. The aim of this research is to gain insight in the rheology of the lower crust and the upper mantle by investigating the xenolith microstructure. Microstructural observations have been used to determine the dominant deformation mechanisms. Differential stresses were estimated from recrystallized grain size piezometry of plagioclase and clinopyroxene for the lower crust and olivine for the upper mantle. The degree of deformation can be inferred from macroscopic foliations and the deformation microstructures. Temperature for one sample was estimated using microprobe analyses, and water content was measured for three samples using Fourier infrared spectroscopy. Results show that both the lower crust and the upper mantle have been affected by multiple stages of deformation and recrystallization. In addition the dominant deformation mechanism in both the lower crust and the upper mantle is dislocation creep based on the existence of strong crystallographic preferred orientations. The differential stress estimates for the lower crust are 10–30 MPa using plagioclase and clinopyroxene paleopiezometry. For the upper mantle, the differential stress estimate is 30 MPa. These results indicate that the strength of the lower crust and the upper mantle are very similar. Our data do not fit with the general models of lithospheric strength and may have important implications for the rheological structure of the lithosphere in transtensional plate margins and for geodynamic models of the region.

Contents

Introduction

The rheology of the lower crust and the upper mantle is difficult to constrain, due to restrictions imposed on the direct observation of these lithospheric levels. The mechanical behaviour of the lower crust and upper mantle, however, is critical for understanding the rheological stratification of the lithosphere and the relative strength of the different lithospheric layers, which in turn are important to determine the occurrence and nature of plate tectonics. Understanding plate tectonics is crucial for constraining time-dependant deformation and hazard along active fault zones [Bürgmann & Dresen, 2008]. Distribution of rheological properties and strength in the lithosphere are still strongly debated [Bürgmann & Dresen, 2008; Behr & Hirth, 2014; Gueydan et al., 2014].

Experimental deformation studies have provided significant insights into the rheology of the lower crust and upper mantle. [e.g. Byerlee, 1978; Brace & Kohlstedt, 1980; Hirth and Kohlstedt, 2003]. However, many of these experimental studies have extrapolated flow laws based on strain rates and stresses that are usually much higher in experiments than they are in nature because of time restrictions. To get more reliable data experimental deformation data can be used in conjunction with natural samples to estimate stress in the lithosphere. Extrapolating experimentally-derived flow laws to naturally deformed rocks in the lower crust and upper mantle requires knowledge of the rock type, deformation mechanism, grain size, water content, thermal gradient, and scales of localization.

Crustal and mantle xenoliths extracted from recent basaltic lavas that were erupted in active tectonic regions can provide an exceptional opportunity to correlate the present-day with active tectonic processes. This comparison can help to determine: 1) the relative strength between the lower crust and upper mantle; 2) where the peak strength is expected; and 3) the rheological interactions between the different lithospheric expected [Brace & Kohlstedt, 1980; Molnar, 1992; Mehl & Hirth, 2008; Thatcher & Pollitz, 2008; Behr & Hirth, 2014; Behr & Platt, 2014; Chatzaras et al., 2015].

The San Quintin volcanic field in Baja California, Mexico, comprises a key location for studying the rheology of the lithosphere (figure 1). Erupted lavas in this active rift system carry upper mantle and lower crustal xenoliths. The Gulf of California formed by the relative tectonic movement between the Pacific, Farallon and North American plates and comprises a trans-tensional rift zone. Complex interaction between the tectonic plates caused a transition from continental extension in the north to oceanic spreading accommodated by transform faults, in the south [Stock & Hodges, 1989; Atwater & Stock, 1998; Nagy and Stock, 2000; Zhang et al., 2007; Zhang et al., 2009; Palasse et al., 2012].

In this study we investigated the microstructures in one mantle xenolith and twenty-four lower crustal xenoliths from the San Quintin volcanic field in Baja California, to obtain more insights into the rheological properties of the continental lithosphere in this actively deforming region (figure 1). The lower crust is the main focus of this study as it is the least constrained layer in the area in terms of rheology. Evidence from the xenoliths helps us to constrain differential stresses, strain rates, viscosities, temperatures and water content in the lower crust and upper mantle. The parameters all influence the large scale deformation in the actively deforming Gulf of California.

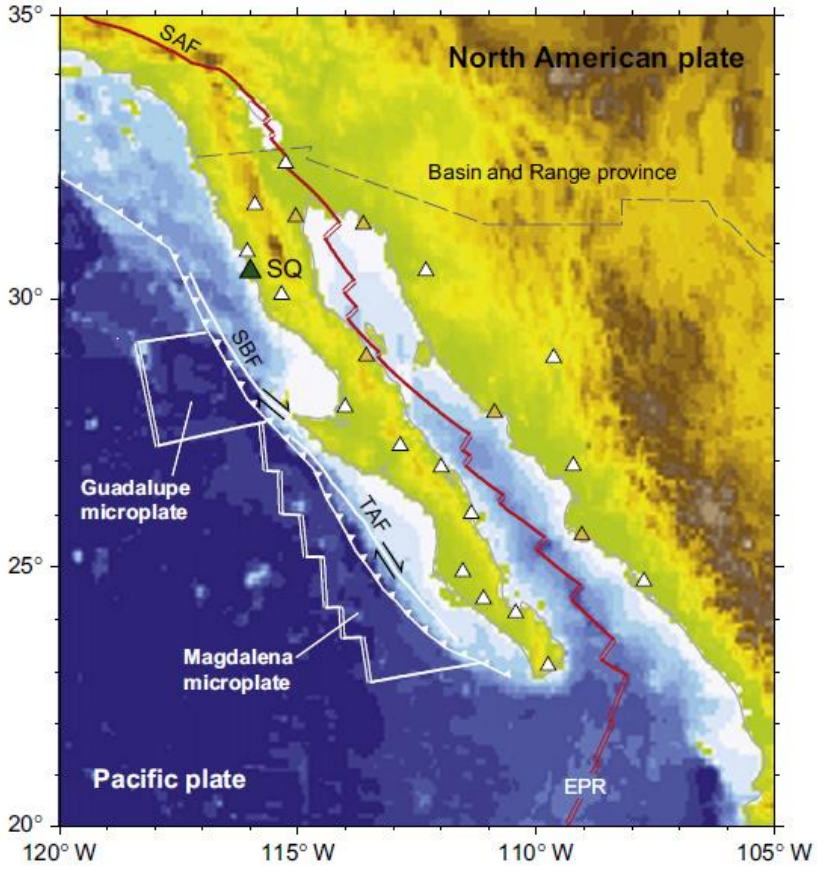

Figure 1: tectonic sketch map of the Gulf of California rift system. The location of the San Quintin volcanic field (SQ) is indicated on this map to show where the xenoliths have been collected. The present-day plate boundaries between the North American and pacific plate are shown. In addition two subducted microplates that are relics from the Farallon plate are also indicated. SAF: San Andreas Fault, EPR: East Pacific Rise, SBF: San Benito Fault, TAF: Tosco Abreojos Fault. Triangles show the locations of the NARS-Baja seismic network [Zhang et al., 2007; Palasse et al., 2012].

Geological Setting

Tectonic Setting

Oblique movement of Baja California away from North America during the last six million years led to the opening of the Gulf of California [Wang et al., 2009]. The Gulf of California is still an active extensional rift system that forms part of the boundary between the Pacific and North American plates, linking the East Pacific Rise with the San Andreas transform fault system (figure 1) [Zhang et al., 2007; Zhang et al., 2009]. The rift system in the Gulf of California changes from an oceanic-type spreading centre and transform fault system in the south to a region of diffuse continental extensional deformation in the north [Nagy and Stock, 2000]. Figure 2 shows the tectonic map of the evolution of the rift system in the last six million years. The trans-tensional rift system is the result of a complex interaction between the Farallon, Pacific and North American plates.

The complex interaction between the three plates can be divided by three phases that has evolved the Pacific-North America plate boundary to its current rift system [Nagy & Stock, 2000]. The first tectonic phase resulted in subduction of Farallon plate fragments beneath North America. The Farallon plate started to break up just after 28 Ma when the Pacific-Farallon divergent plate boundary approached the Farallon-North America subduction zone (figure 3). The break-up of the Farallon plate resulted in coupling between the Pacific and North America plates which led to the broad transmission of NW directed movement of the Pacific through the western United States. This movement produced diffuse

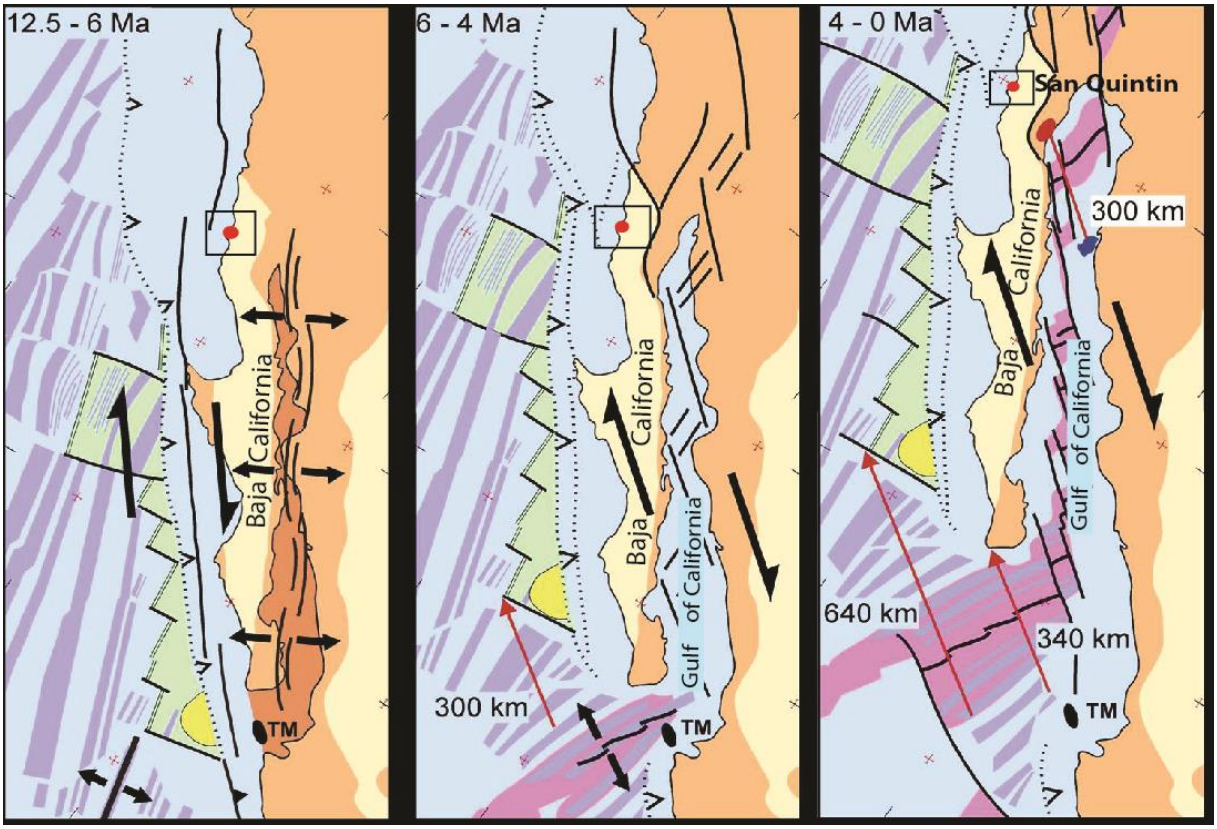

Figure 2: Tectonic map of the opening of the Gulf of California in the last 12.5 million years. The Gulf of California started opening at ~5.5 Ma when the transform faults in the west started to move inlands in the weakened proto-gulf. The transform faults started in the mouth of the Gulf of California and slowly moved northwards in the last 4 Myr. The green areas show the location of subducted microplates [after Fletcher et al., 2007]

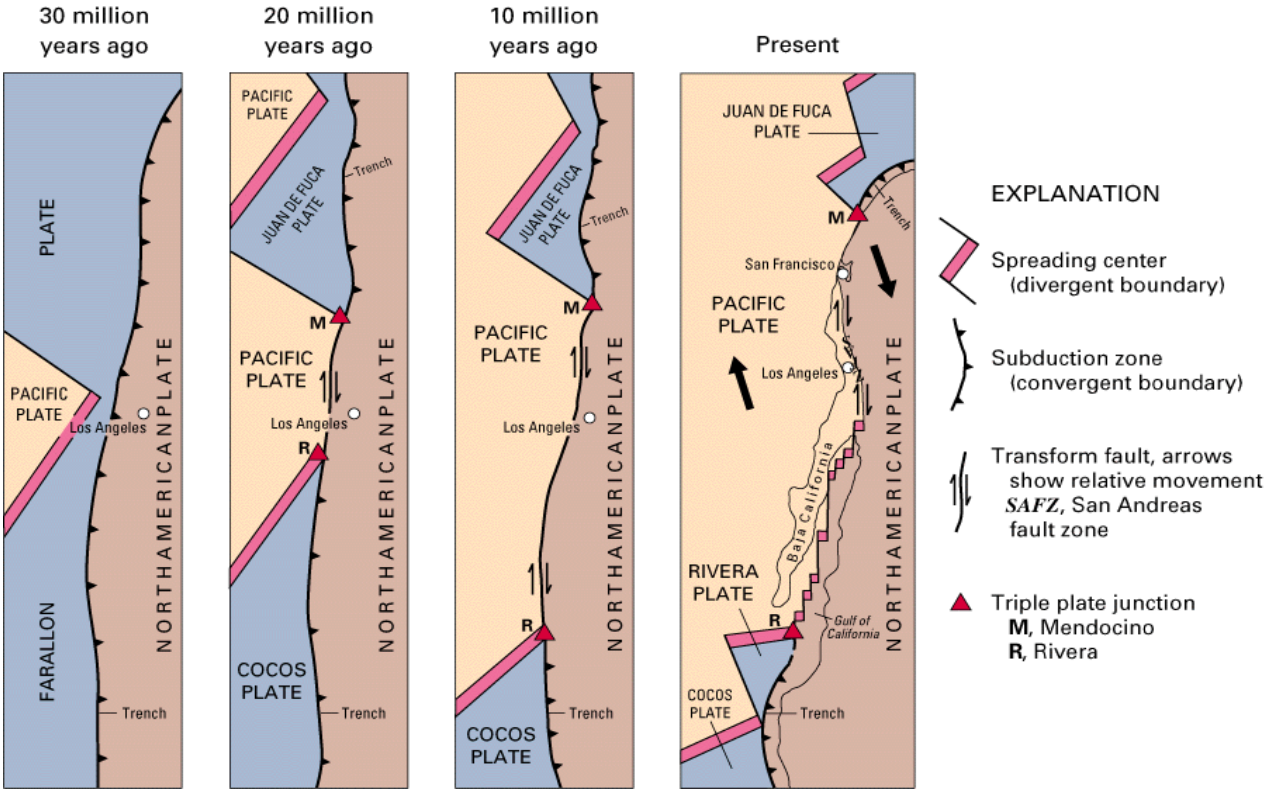

Figure 3: Tectonic maps of the interaction between the Pacific, North American and Farallon plates in the last 30 Myr. At 28 Ma the Pacific-Farallon divergent plate boundary approached the North American-Farallon subduction zone. This caused the Farallon plate to break up and the Pacific and North American plates to be coupled. Coupling continued as the triple plate junctions moved northwards and southwards [USGS].

basin-and-range-type deformation. After the coupling between the Pacific and North America plates the triple junction between the Farallon, Pacific and North America plates (called the Rivera triple junction) migrated southwards along the western side of the Baja California peninsula. This southward movement of the Rivera triple junction replaced the Farallon-North American convergence by the Pacific-North American transform motion. Due to this process the Farallon plate continued to fragment into multiple microplates such as the Guadalupe and the Magdalena microplates that have been found offshore the Baja California peninsula (figure 1) [Stock & Hodges, 1989; Atwater & Stock, 1998; Nagy & Stock; 2000; Zhang & Paulssen, 2011]. Subduction of the fragmented Farallon plate ceased at around 12 Ma [Michaud et al., 2006].

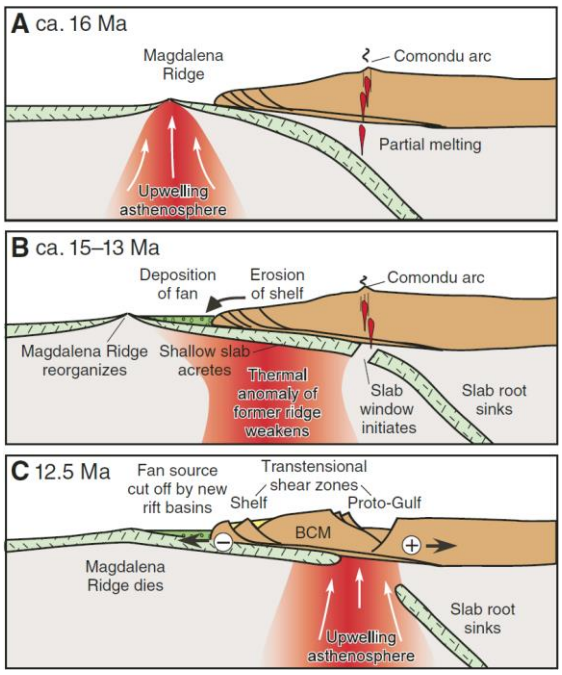

Figure 4: Cross sections displaying the tectonic evolution of the Magdalena shelf during the last 16 Myr. (A) Magdalena ridge converges on the trench east of Baja California at ~16 Ma. (B) Between 15-12 Ma subduction between the North American and Farallon plate ended and the transform motion between the Pacific and North American plate took over. (C) The extension component of this motion was concentrated on the thermally weakened Comondu arc after 12.5 Ma which led to the formation of the proto-Gulf [Fletcher et al., 2007]

The second tectonic phase comes after subduction had ended. After subduction the transform motion between the Pacific and North America plates was partitioned mostly along the right-lateral San Benite and Tosco-Abreojos fault zones (figure 1&2) [Zhang & Paulssen, 2011]. The extension component caused by this motion was accommodated by a broad region which included a large zone thermally weakened by back arc extension induced by Miocene subduction (figure 4). The thermally weakened region formed the proto-Gulf which separated the Baja California Range to the west and the Sierra Madre Occidental to the east [Nagy & Stock, 2000; Zhang & Paulssen, 2011]. The San Benite and Tosco-Abreojos fault zones remained active until at least 5.5 Ma.

The third tectonic phase describes the formation of the Gulf of California during the latest Miocene to present day (figure 2). At around 5.5 Ma a NW-SE directed extension began in the mouth of the Gulf. This extension at the mouth of the Gulf caused brittle stretching in the upper crust and ductile stretching in the lower crust. After 1.5 Myr transform faults had moved northwards along the length of the Gulf (figure 2). Pull-apart basins formed at step overs between these newly formed transform faults and consequently the Gulf of California had started to open. This motion is still active, although the direction became slightly more E-W orientated after 3.5 Ma, and has taken up around 90% of the Pacific-North American plate motion [Nagy & Stock, 2000; Zhang & Paulssen, 2011].

Influence of the crust

Baja California remained relatively unaffected by the deformation that led to the formation of the Gulf of California. Localization of rifting in the Gulf of California can be attributed to: 1) the plate geometry of rifting; 2) pre-existing structure of the rift zone. [Langenheim & Jachens, 2003]. The crust of the Baja California may have acted as a pre-existing structure. The basement rocks of the Baja California consist of the Jurassic-Cretaceous Peninsular Ranges batholith (PRB). This batholith is well exposed at the surface in parts of the Peninsular Ranges, and has an axially distinct western (WPRB) and eastern (EPRB) zones (figure 5). These zones are differentiated based on age, petrology, style and depth of emplacement, prebatholithic wall rock, and geophysical criteria [Gastil, 1975; Kimbrough et al., 2001]. The WPRB consists of gabbro and monzogranite and intruded the lower crust between ~140 – 105 Ma.

Furthermore the WPRB rocks were affected by sub solidus ductile deformation. The EPRB exists mostly out of tonalite and low-K granodiorite that outcrop as a series of large nested intrusive centres. In addition there are also smaller intrusions that are named the La Posta intrusions. Stratigraphic record shows that the EPRB was emplaced by massive intrusion between ~100 to 90 Ma [Gastil, 1975; Kimbrough et al. 2001]. All the batholith intrusions have been affected by compressional deformation, related to the subduction of the Farallon plate beneath the North American plate [Gastil, 1975]. Magnetic

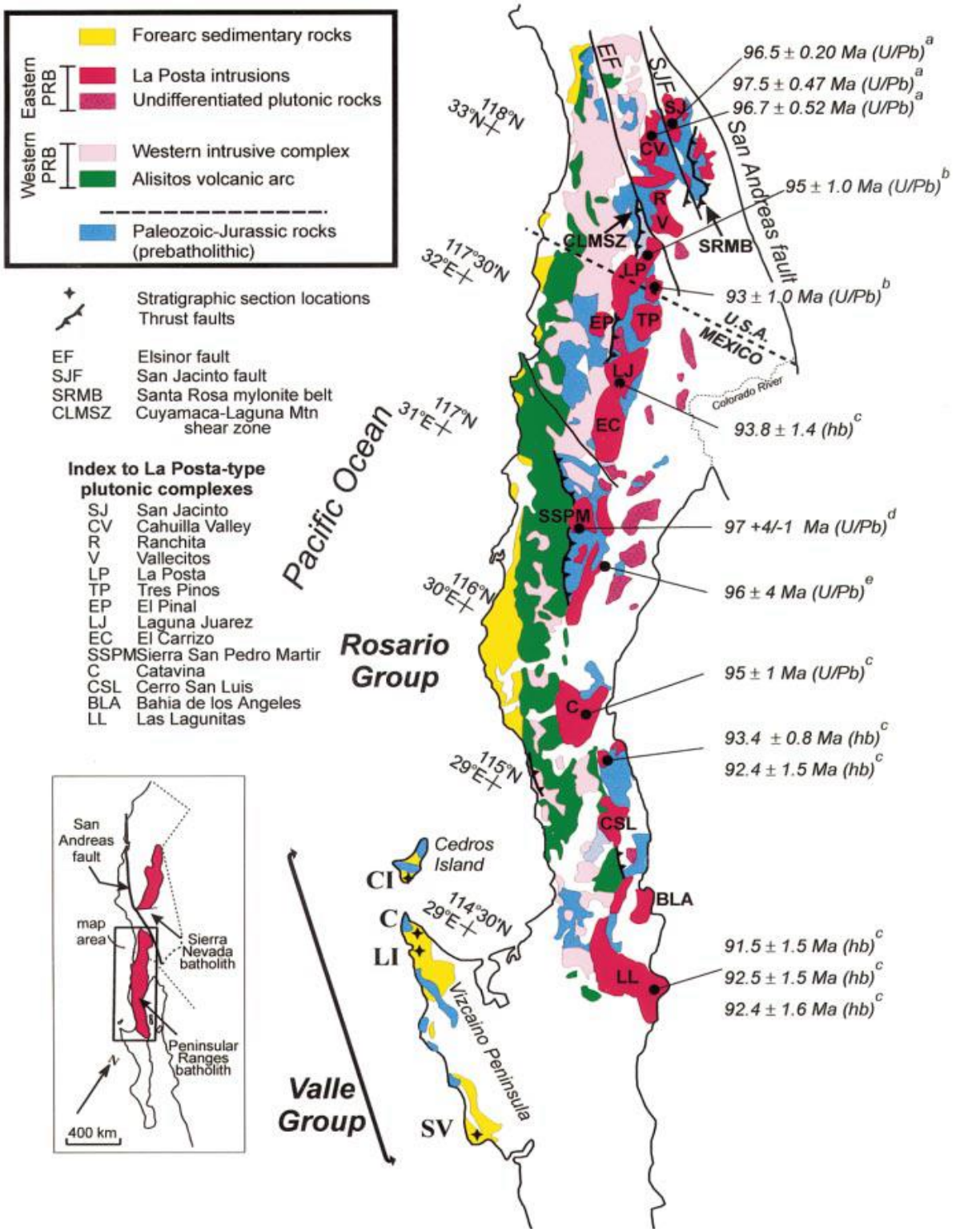

Figure 5: Geological map of the Baja California. The Western Peninsular Ranges Batholith is shown on the map with green and pink. The Eastern Peninsular Ranges Batholith is shown on the map with red and dark pink. The ages of intrusion are displayed at the location from which they were measured [Kimbrough et al., 2001].

data show that the more mafic WPRB crust beneath Baja California has a relative coherent structure [Langenheim & Jachens, 2003]. The Baja California Peninsular is bounded by extensional and strike-slip faults on the west and rifting on the east, whereas the WPRB has been affected by limited faulting that have no major offset. It is therefore likely that the WPRB acted as a rigid block, influencing the location of continental rifting and therefore the formation of oceanic crust in the Gulf of California.

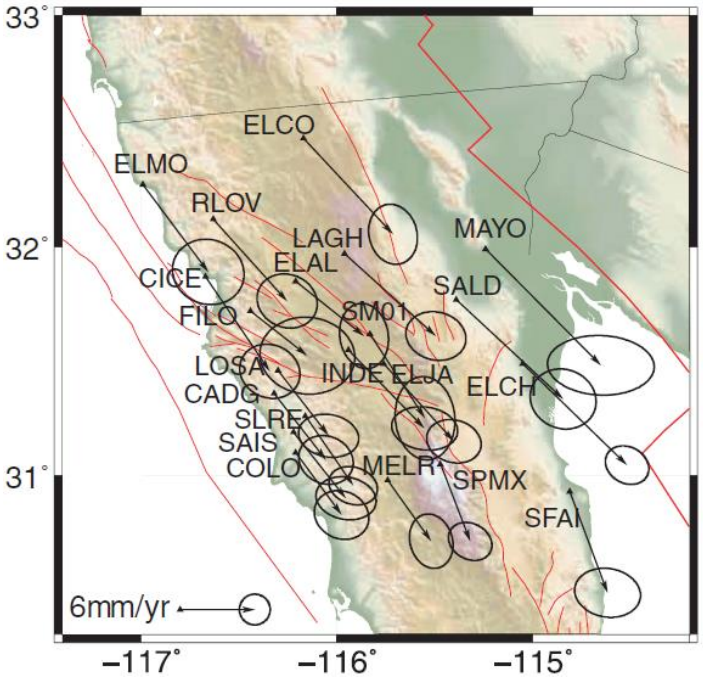

Figure 6: GPS network on the northern Baja California. The velocity is relative to the Pacific plate. The circles represent the error intervals [Plattner et al., 2007]

Crustal thicknesses in the Gulf of California region have been mapped using receiver functions revealing significant lateral variations. The crust is thinner in the EPRB and the Gulf Extensional Province ranging between 21 and 27 km in a strip of 50 km along the eastern Baja California peninsula. The WPRB is much thicker ranging from 32 to 37 km [Persaud et al., 2007]. It remains unclear when the thinning of the EPRB occured but the two possible scenarios are during: 1) during subduction (before 16 Ma); or 2) during the opening of the Gulf of California (after 5.5 Ma) [Persaud et al., 2007].

Even though the WPRB has acted as a rigid plate there is still some movement of the northern Baja California relative to the Pacific plate (4-6 mm/year) (figure 6) [Plattner et al., 2007]. This makes it likely that there is still deformation going on in the crust beneath the Baja California.

The mantle beneath Baja California and the Gulf of California

Seismic research has revealed much about the mantle behaviour below the Gulf of California region. The Gulf of California is probed by a great number of seismometers which are used to provide a high horizontal resolution of the mantle. Rayleigh-wave tomography was used to image the shear velocity of the upper ~200 km of the mantle. Figure 2 shows the shear velocity anomalies averaged over the depth of 50 to 90 km. The low velocity anomalies are linked to the dynamic buoyancy-driven upwelling and melting which were initially formed due to extension that opened the Gulf. There is a clear difference in shear velocities between northern and southern Baja California. The high anomalies in southern Baja California are thought to be due to a remnant of a Farallon slab fragment [Wang et al., 2009; Zhang et al., 2009; Zhang & Paulssen, 2011].

In addition to the seismic research a microstructural investigation was conducted on the upper mantle xenolith, extracted from the San Quintin volcanic field. The xenoliths used for the microstructural investigation of the upper mantle come from the same volcanic centres as the xenoliths we use in the present work. The xenoliths show strong presence of upper mantle deformation and recrystallization, which seems to reduce with depth [Palasse et al., 2012]. The water content in the xenoliths was measured by perlier et al., [2002] and peslier and Luhr [2006]. The upper mantle xenoliths contain 77-154 ppm H_2O by weight for the whole rock, 0-6.6 ppm for olivine and 38-477 ppm H_2O by weight for pyroxene. The olivine water content is too low for wet deformation so the xenoliths have been developed in dry conditions. A strong presence of crystallographic preferred orientation (CPO) suggests dislocation creep as the main deformation mechanism in the upper mantle. Strain rates are estimated to be 1.1-5.7 x 10^{-14} s^{-1} for a 1 km thick shear zone and 1.1-5.7 x 10^{-15} for a 10 km thick shear zone. Flow stress calculated from olivine grain sizes ranges between 10 and 30 MPa and flow stress from dry flow laws are 10 to 40

MPa. The viscosity of the shear zones in the upper mantle which is 4.4 x 10^{19}-3.5 x 10^{20} and 4.4 x 10^{20} – 3.5 x 10^{21} for 1 km and 10 km thick shear zones respectively. The low viscosity suggests the presence of a relative weak upper mantle and that the high viscosity mechanical lithosphere is restricted to the crust [Palasse et al., 2012]

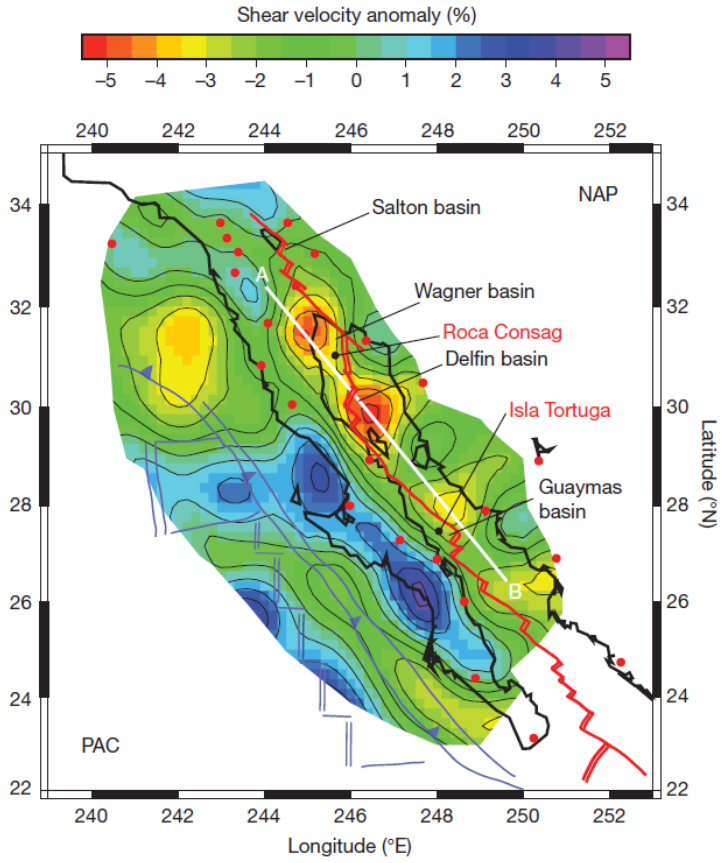

Figure 7: Average shear velocities of the upper mantle at a depth of 50 to 90 km beneath the Baja California and Gulf of California regions. Negative anomalies correspond to slow regions. The contour line interval is 0.5%. The thick black lines represent the coast lines, the light blue lines indicate the positions of fossil spreading centres, trenches and strike-slip faults west of Baja California. The red lines shows the active plate boundary [Wang et al., 2009].

Strength contrast between lower crust and mantle

The relative strength of the crust and upper mantle has been a long standing question and topic of debate in tectonic studies [Burov & Watts, 2006; Burgmann & Dresen; 2008; Thatcher & Pollitz, 2008; Vauchez et al., 2012; Behr & Hirth, 2014; Gueydan et al., 2014].Varying views resulted in three first-order models of strength through the continental lithosphere. The models have been named after different deserts to describe the how the strength of the different rheological layers is distributed within the continental lithosphere. Figure 3 shows a schematic view of the three prevalent rheological models of the lithosphere.

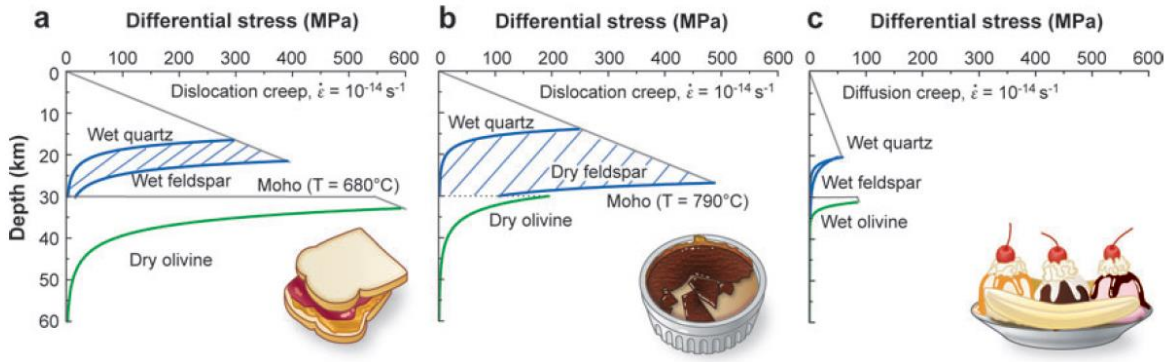

Figure 8: Schematic view of the three most common first order rheological models of the continental lithosphere under a strain rate of 10^{-14} s^{-1}. In all three models the upper crust has its frictional strength increased with pressure and depth. (a) The jelly sandwich model has a weak mid-lower crust and a strong mantle composed of dry olivine. (b) The crème brûlée model assumes that the mantle is weak, due to the presence of water and high temperature deformation, and the dry and brittle crust determines the strength of the lithosphere. (c) The banana split model assumes that the lithosphere as a whole has its strength greatly reduced due to various strain weakening and feedback processes [Bürgmann & Dresen, 2008].

The most classical view of the continental lithosphere is involves a strong upper crust and lithospheric mantle with a weak middle and lower crust sandwiched in between. This first model (figure 8a) is often called the jelly sandwich. In this model the upper crust is assumed to be in a state of frictional equilibrium with active faults limiting its strength as described by Byerlee's law [Byerlee, 1978]. The increase in strength of the crust is thought to continue with depth until it reaches the brittle-ductile transition where the strength of the crust is being reduced with further increasing temperature and pressure due to thermally activated creep processes [Goetze & Evans, 1979; Brace & Kohlstedt, 1980]. The lithospheric mantle is composed by ultramafic rocks which generally have higher viscosity due to their higher melting temperatures. According to this model the lithospheric mantle determines the strength of the tectonic plates in long time frames [Bürgmann & Dresen, 2008].
The Jelly sandwich model was rebuked by Jackson [2002] who proposed that the upper crust is controlling the strength of tectonic plates, because the lithospheric mantle was comprises a weak layer due to water presence and deformation at high temperatures [Drury et al., 1991; Bürgmann & Dresen, 2008]. The model of Jackson [2002] was is called the crème-brûlée model by Burov and Watts [2006] (figure 8b). Burov and Watts [2006] have shown, however, that this model cannot explain the presence of long-lived mountain ranges and the integrity of a downgoing slab in collisional systems. The crème-brûlée model and may only apply in a limited amount of tectonic settings (e.g. a young hot rift system). An area for which the crème brûlée model might be applicable is the Mojave region in southern California, where recently exhumed mantle xenoliths have been studied that derived from just below the Moho [Behr & Hirth, 2014].The upper mantle has peak stresses of 13-17 MPa and a mean effective viscosity of 3 x 10^{19} Pa s. The crust is expect to be much stronger with viscosities one or two orders of magnitude higher than that of the upper mantle. Based on records of wet relative un-deformed gabbros flow laws were extrapolated for the lower crust for two strain rates, which resulted in a strong lower crust. In this case the whole crust would be the primary load-bearing layer [Behr & Hirth, 2014].
The last model considers the whole lithosphere as weakened and is called the banana split model (figure 8c) [Bürgmann and Dresen, 2008]. It has been proposed that this model can apply to the lithosphere along plate boundaries where various weakening processes have reduced the strength throughout the entire thickness of the lithosphere. These weakening processes can be due to thermal, fluid and strain effects [Bürgmann & Dresen, 2008]. The San Andreas transform fault has been proposed as an example of the banana split model [Burgmann & Dresen, 2008]. Based on a study of xenoliths extracted from the upper mantle beneath the San Andreas Fault system, Chatzaras et al. [2015] suggest a new rheological model for strike-slip fault zones, named the lithospheric feedback model. This model suggests that the various mantle deformation and the frictional crustal information in strike-slip fault zones are mechanically coupled and have different tendencies. Mantle flow induces widespread deformation in the upper crust, while crustal earthquake rupture localizes deformation in the upper mantle [Chatzaras et al., 2015]. According to the lithospheric feedback model, no strain weakening mechanism is required to explain the deformation at the San Andreas Fault system.

Methods

Sample collection and preparation

The studied lower crustal xenoliths were collected from two northern volcanic centres in the San Quintin volcanic field (figure 9), in Baja California, Mexico by Vasileios Chatzaras. Twenty-four lower crustal xenoliths were collected. Of these xenoliths twenty-eight thin sections of 30 micron thick were produced in the rock cutting lab at UW-Madison. Twenty-four of the lower crustal thin sections were produced on the XZ fabric plane. The XZ fabric plane was determined by visual observation of the rock forming mineral. We also tried to determine the 3D fabric by means of X-ray Computed Tomography and Anisotropy of Magnetic Susceptibility but this had no result. Because of sample size restrictions, thin sections in four xenoliths were produced in random orientations. Appendix A shows a table with all the thin sections and information concerning how they were produced.

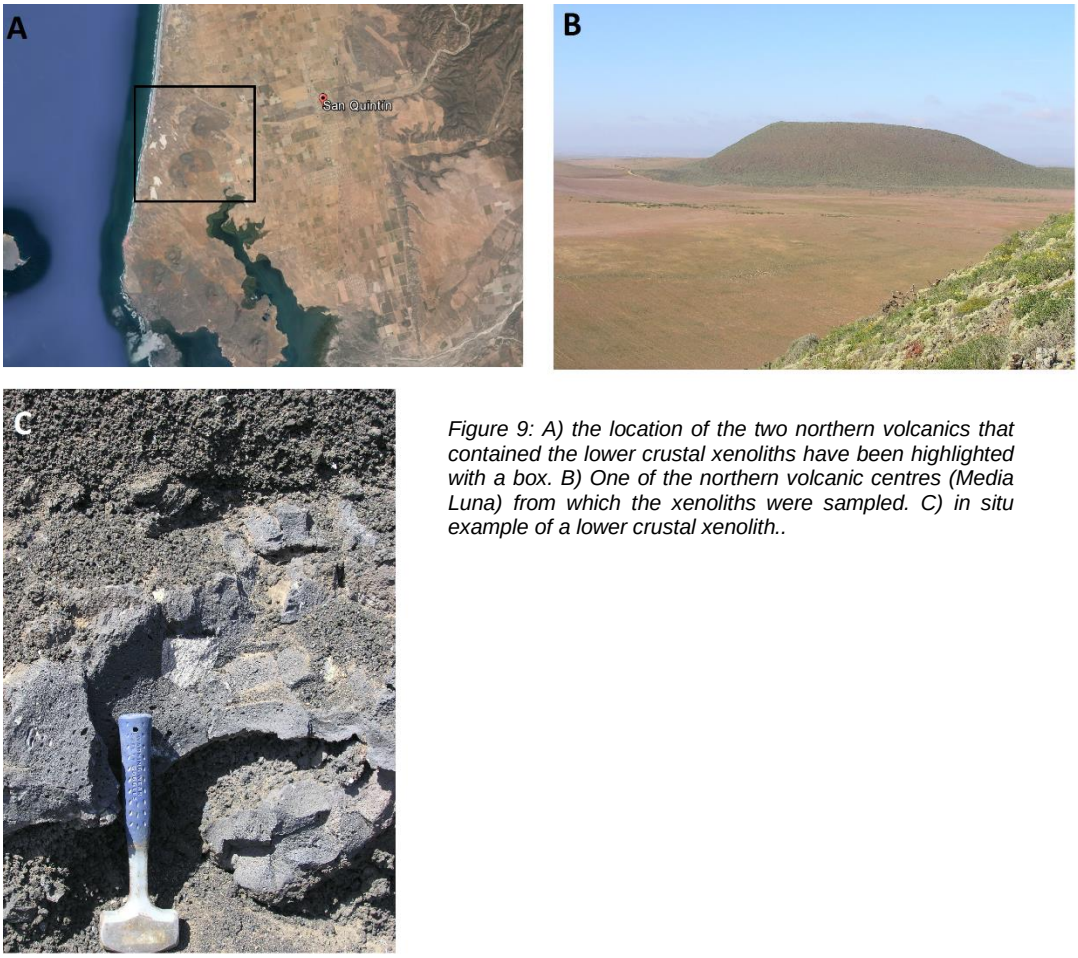

Figure 9: A) the location of the two northern volcanics that contained the lower crustal xenoliths have been highlighted with a box. B) One of the northern volcanic centres (Media Luna) from which the xenoliths were sampled. C) in situ example of a lower crustal xenolith..

Light microscopy

Polarized optical microscopy was used to study the microstructures and petrography of the xenoliths. A polarized microscope has the option to use plain polarized light (ppl), cross polarized light (xpl) and a gypsum plate for analysing the thin sections. To identify which minerals were in the sample ppl was used to determine the pleochroism and the relief of the mineral phases and xpl was used to determine the interference colours of the minerals. Microstructures were mostly studied in xpl because most structures, such as twinning and undulose extinction, are not usually visible in ppl. In addition grain

boundaries of certain phases, like feldspar and quartz, do not have enough relief to be clearly seen in ppl. The gypsum plate was used to see if there is a crystallographic preferred orientation (CPO) in the sample.

Grain size analysis

In order to determine the recrystallized grain size of olivine, plagioclase and clinopyroxene, thin section images have been made using the Leica DMRX light optical polarization microscope in the high pressure/temperature lab of the Earth Sciences Department at Utrecht University. The photomicrographs taken with the Leica microscope were directly transferred to the program QWIN Pro. This software can be used to determine the right focus, as well as to adjust the exposure time, contrast and gamma. Furthermore the software allows for adding a scale bar to the photomicrographs. Photomicrographs were taken from areas that included dynamically recrystallized grains with a minimum second phase amount. For samples SQ-16, SQW-75, SQW-110 and SQL-48 a collage of multiple photomicrographs were made to acquire grain sizes from a larger area of interest.
Grain boundaries of olivine, plagioclase and clinopyroxene included in a photomicrograph were outlined using the drawing tool in adobe illustrator. During this process the distinction between recrystallized grains and relic grains was not yet made. An example of this is shown in Figure 10. Secondary phases that were included between grain boundaries were filled in with the same colour as the grain boundaries. The resulting images containing solely the outlines of the grains that have to be measured are imported into ImageJ. Lines around the grains were made as thin as possible for ImageJ to register it as a closed line to avoid affecting the grain sizes with width of lines.

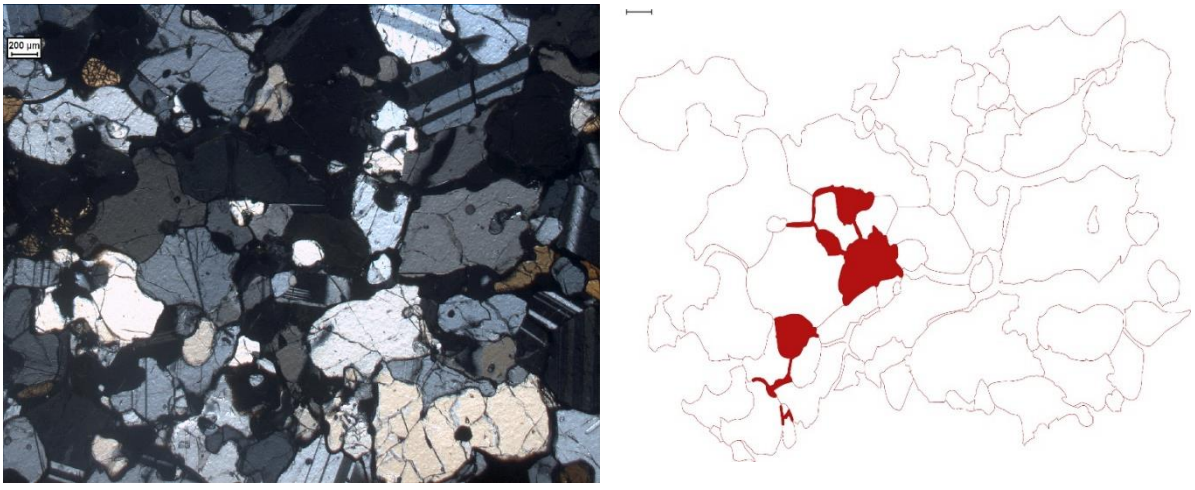

Figure 10: The left image shows a cross polarized light photo of an area in section SQW-76. The recrystallized grain size of plagioclase was measured in this sample by drawing lines around the grains in adobe illustrator as shown in the right image. Secondary phases that get enclosed by the drawn grain boundaries are filled in with the same colour as the lines so they can be skipped while applying a threshold in imageJ.

ImageJ is an image analysis software. The analysed photomicrograph was scaled relative to the original size, and a threshold was set for analysing the area inside the grain outlines. After thresholding the image the areas of the grains were measured. The calculated areas were then imported into excel from where the diameter of the grains were calculated using a simple equation:

$$d = 2\sqrt{\frac{A}{\pi}} \qquad (1)$$

where d is the diameter in µm and A is the area in μm^2. This method calculates the diameter of a circle with area equal to that of the grain. A correction factor of 1.2 [van der Wal, 1993] must be applied to

the calculated diameters to adjust for not knowing where the 2D section is located in the assumed circulargrain. This is explained in figure 11.

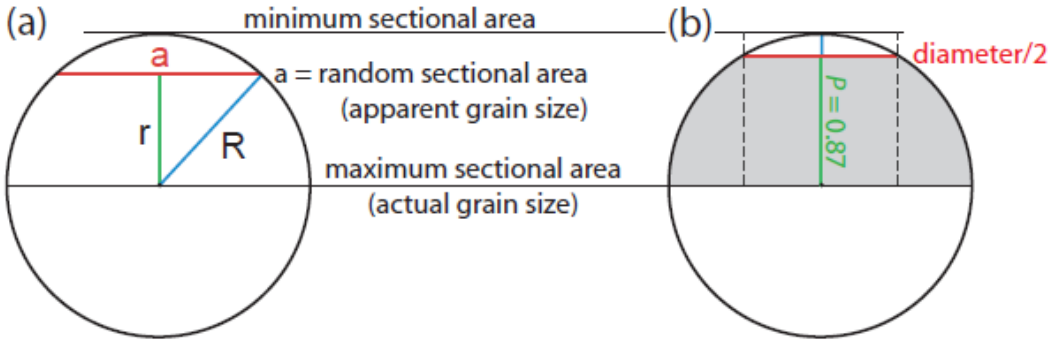

Figure 11: Schematic view of a grain showing why a correction factor has to be applied to the calculated grain sizes. A) a is a possible section through a grain that displays the apparent grain size. B) The section a through the grain is shown as only a half of the true diameter. The actual diameters measured from a section like a can vary anywhere between 0 and the maximum sectional area and a correction is needed to get a respectable distribution [Lopez-Sanchez & Llana-Fúnez, 2015].

Bins or size groups (e.g. 100-200 μm) were made for each sample in excel and the corresponding frequencies of grains belonging to a bin were calculated. The data were used to create histograms to view the grain size distribution in each sample. The recrystallized grain size is required for Paleopiezometry but all grains have been measured. Therefore a cut-off values must be determined for each sample. We did this by looking at the microstructures of the grains (e.g. straight or lobate boundaries). The smallest grain size of the smallest grain that was not considered recrystallized (if any) was used as a cut-off value. Finally the geometric means were calculated for each sample to compare with the histograms and to use in the piezometers to estimate paleostress.

Paleopiezometry

At high temperature and pressure conditions, minerals and rocks behave in a ductile way and flow in response to the applied deviatoric stress. Ductile deformation is accommodated by the motion of vacancies and dislocations [Poirier, 1985]. Structural features of deformed rocks vary with the magnitude of the applied differential stress. These are: 1) Dislocation density; 2) the mean sub-grain diameter; and 3) the mean dynamically recrystallized grain size. These features can therefore provide a means with which you can estimate paleostress. Recrystallized grain size is the most used microstructural feature to measure flow stress in shear zones as it easy to measure and relatively reliable compared to the other structural features [Post & Tullis, 1998; Lopez-Sanchez & Llana-Fúnez, 2015]. However, when measuring flow stress it is assumed that the sampled rocks deformed under dislocation creep under constant stress and that they reach a mechanical stead-state creep. If this is true than deformed rocks will generally have a stable mean grain size [Michibayashi, 1993] Relation between the recrystallized grain size and differential stress is usually given as:

$$D = K\sigma^{-p} \qquad (2)$$

Where D is the mean recrystallized grain size, σ is the flow stress and K and p are material parameters usually obtained by fitting the experimental data [Twiss, 1977].
The lower crustal samples consist mostly out of plagioclase and clinopyroxene. The theoretical paleopiezometer of Twiss [1977] is still widely used to estimate the paleostress of feldspars [Rybacki & Dresen, 2004; Burgmann & Dresen, 2008; Mehl & Hirth, 2008; Michibayashi et al., 2014] and will be used in this study for the recrystallized grain size of plagioclase. The paleopiezometer that Twiss proposes relies on the assumption that the formation of subgrains and recrystallized grains are energetically favourable processes. If this assumption is correct that would mean that the total strain

energy of dislocations ordered into a subgrain or recrystallized grain boundary must be either less or equal to the steady state density within an enclosed volume. This relation indicates that there must be a unique grain size at which both energies are equal because if the grain size changes the grain boundary energy changes with surface area (d^2) and the total volume energy changes with volume (d^3). This is expressed for a cubic subgrain or recrystallized grain as:

$$6\gamma d^2 = w\rho d^3 \tag{3}$$

Where γ is the dislocation strain energy per unit area in the grain boundary, w is the dislocation strain energy per unit length in the grain volume, d is the grain dimension and ρ is the steady state dislocation density in the grain volume.
Stress can be added to the expression by relating differential stress to dislocation density which leads to:

$$\sigma = \alpha \Gamma b \rho^{\frac{1}{2}}, \quad \Gamma \equiv \frac{\mu}{1-v} \tag{4}$$

Where α is an empirical parameter of order 1, b the Burgers vector, ρ the steady state dislocation density in the grain volume, σ the differential stress, μ the shear modulus and v Poisson's ratio.
By assuming that all dislocations are edge dislocations, all boundaries are simple tilt boundaries and that crystals are elastically isotropic, relatively simple equations can be set up for volume and boundary energy densities:

$$\frac{\sigma}{\Gamma} = K(\frac{d}{b})^{-p} \text{ or } \log\frac{\sigma}{\Gamma} = log\ K - p\ log\ \frac{d}{b} \tag{5}$$

Where

$$p \equiv \frac{\theta}{2\theta-1}, \qquad logK = p[log\frac{3e\alpha^2\beta}{\pi\theta} - \frac{1}{\theta}log\frac{\alpha\beta}{2}] \tag{6}$$

In these equations θ is the ratio of total dislocation length in the boundaries to the dislocation lengths in the enclosed volumes. β is a value that corrects for the energy of the dislocation core and e is the Napierian base.
θ is the only parameter that has a different value for subgrains and recrystallized grains. Under the assumption that the smallest stable grain size is likely to develop, θ for a dislocation free recrystallized grain was estimated to be between 1.4 and 2. This gives a p value between 0.67 and 0.78 for recrystallized grains. By plotting data sets on the variation of stress with recrystallized grain size on non-dimensional coordinates for a number of different phases it was that:

$$p = 0.68 \pm 0.02 \quad , \qquad logk = 0.38 \pm 0.01 + 3.85\Delta p \tag{7}$$

Substituting equation (7) into equation (5) gives the following equation for recrystallized grain sizes:

$$log\frac{\sigma}{\Gamma} = 0.38 - 0.68log\frac{b}{d} \tag{8}$$

This equation can be rewritten as:

$$\sigma = Bd^{-0.68} \quad \text{With} \quad B \equiv K\Gamma b^p \tag{9}$$

Where d is the recrystallized grain size in μm and σ is the differential stress in MPa. The preexponential component B for plagioclase is generally taken as 7.8 under high temperature conditions [Chen et al., 2007; Mehl & Hirth, 2008; Michibayashi et al., 2014]. This component can be altered if the slip system is known [Mehl & Hirth, 2008; Homburg et al., 2010].

The theoretical piezometer of Twiss [1977] is not the only piezometer for plagioclase. Post and Tullis [1999] have experimentally calibrated a recrystallized grain size piezometer for low temperature migration recrystallization in feldspar. They deformed albitic feldspars under simple shear and axial compression at a temperature of 900 °C and a confining pressure of 1500 MPa. The results of these experiments yield the piezometric relationship:

$$\sigma = (\frac{55}{d})^{1.515}$$

Where d is recrystallized grain size in μm, and σ is the flow stress in MPa.

Because clinopyroxene is also a major phase in the lower crustal rocks and the theoretical study of Twiss [1977] is very controversial (see discussion) and the Post and Tullis [1999] piezometer is meant for low-temperature miggration, an additional paleopiezometer for the recrystallized grain size of clinopyroxene has been applied for comparison of the paleostress estimates. Avé Lallement [1978] experimentally deformed a single crystal of diopside as well as polycrystalline websterite. Experiments were carried out with temperatures from 200º to 1050° C, strain rates of roughly 10^{-3}-10^{-6} sec^{-1}, and confining pressures of 5-15 kb (using talc as a pressure medium). The experiments were mostly performed using one set of conditions (strain rate was always kept constant) and revealed a relation between differential stress and recrystallized grain size [Avé Lallement, 1978]. Mercier [1985] later used the data from these experiments to develop a paleopiezometer for clinopyroxene:

$$\sigma = 9.45d^{-1.11} \quad (10)$$

Where d is the recrystallized grain size in μm and σ is the differential stress in GPa. These clinopyroxene experiments have been conducted with older solid-medium deformation apparatus which may have overestimated the stress levels [Green & Borch, 1989, van der Wal et al., 1993]. However, the experimental piezometer of Twiss [1977] gives the lower bound paleostress [de Bresser et al., 2001]. Therefore combining the results of the two may give a lower and upper bound of the flow stress in the lower crust.

The upper mantle xenolith used in this study, predominantly contains recrystallized olivine grains. Olivine constitutes the prevalent upper mantle phase and has therefore been the subject of many experiments concerning the relationship between recrystallized grain size and differential stress [Karato et al., 1980; van der Wal et al., 1993]. We used the van der Wal et al. [1993] paleopiezometer for olivine. Their stress – recrystallized grain size relationship was obtained by studying two natural olivine rocks. The deformation experiments conducted on these rocks was done at confining pressures of 300 MPa, temperatures of 1100° to 1400° C and strain rates of 10^{-4} to 10^{-6} s^{-1}. Both wet and dry experiments were conducted under these conditions to study the influence of water content on the recrystallized grain size. Data from these experiments and previous studies resulted in the following stress – grain size relationship:

$$D = 0.0015^{+0.0004}_{-0.0003}\sigma^{-1.33\pm0.09} \quad (11)$$

Where D is the recrystallized grain size in meters and σ is the differential stress in MPa. The data from this study as well as that of Karato et al. [1980] suggest that the recrystallized grain size seems relatively independent of water content and temperature.

Recrystallized grain size is very sensitive to differential stress [Twiss, 1977; van der Wal et al., 1993] it is therefore important that grain sizes are not altered after deformation. Grain sizes may increase after deformation due to annealing and grain growth, if the temperature remains high. This process called static recrystallization [Twiss, 1977]. Larger grain sizes due to static recrystallization lead to lower stress estimates when using paleopiezometers [Twiss, 1977]. In contrast, an abundance of second phases can lead to limitation of the grain growth during recrystallization. Limited grain sizes will lead to an overestimation of the differential stress when using paleopiezometers [Olgaard, 1990].

Scanning electron microscopy

Scanning electron microscopy (SEM) has been used to get qualitative mineral compositions and to visualize possible reactions or other relationships between mineral phases using density contrast. Thin sections were carbon coated to allow SEM analysis using a JEOL Tabletop SEM type JCM 6000 in the Electron Microscopy facility at Utrecht University with an acceleration voltage of 15 kV. Back-scattered electrons (BSE) were used to create atomic number(Z)-contrast images with a magnification generally higher than 4000x. The energy dispersive x-ray (EDX) spectrometer was to get qualitative measurements of the compositions in a sample. These EDX analyses were done as spot analysis, where it is possible to analyse a specific point on the area of interest to get the x-ray spectra, or by elemental mapping where the whole area of interest is analysed and mapped for each specific element selected. In addition to the table top SEM at Utrecht University a session was also done on the FEG SEM in the biodiversity centre at Naturalis in Leiden to acquire more accurate and precise measurements of the compositions of the samples that were selected for electron microprobe analysis.

Water content

Water content was measured for three of the samples analyzed for grain size analysis. New sections were produced for Fourier transform infrared spectroscopy (FTIR). The thickness of the sections was around 500 μm to match the average diameter of the grains in the sample. This is to limit the influence of water present in grain boundaries as only the water present in the internal structure of the minerals is relevant for the water content during dislocation creep. The samples were polished on both sides and were glued on a glass. To remove the glass the samples were put in acetone for over 24 hours to dissolve the glue.

The infrared spectra were measured for individual grains using a JASCO-IRT-30 infrared microscope that is attached to a JASCO FT/IR-470 plus FTIR spectrometer located in the high pressure/temperature lab of the Earth Sciences Department at Utrecht University. The microscope is equipped with a Mercury Cadmium Tellurium (MCT) detector with liquid nitrogen Dewar. The sample stage is built into a box that is constantly supplied by nitrogen gas during the measurements to reduce the influence of CO_2 gas and H_2O vapour. The samples were not orientated and the IR light was unpolarised. An aperture of 30x30 μm was used for selecting areas free of cracks, inclusions and boundaries under the microscope. Infrared spectra was first taken without the samples to remove the background measurements. The spectra were measured by 150 scan times in the wavenumber range of 1 cm^{-1} to 4000 cm^{-1} with a resolution of 4 cm^{-1} at room temperature. Spectra were taken for different grains of the same phase to see if results are consistent with each other. The direct analysis of the obtained spectra (peak height and area below the peaks) was done with the JASCO software.

To assess qualitatively the water content, we used the Beer – Lambert law:

$$c = \frac{18.02A}{\rho t \varepsilon \gamma} 10^3 \qquad (12)$$

Where c is the water content in ppm, 18.02 is the molecular weight of water, A is the integral area (cm^{-1}) of the absorption bands, ρ is the density of the sample (g cm^{-3}), t is the thickness of the sample, ε is the molar absorption coefficient (L (mol H_2O $cm^2)^{-1}$) and γ is the orientation factor.

The wavelength range in which water can be observed in the spectra is between 3000 and 3800 cm^{-1} for both plagioclase and clinopyroxene [Xia et al., 2006]. The integral molar coefficient is 38,300 L (mol H_2O $cm^2)^{-1}$ for cpx [Rossman et al., 1995] and 107,000 for plagioclase [Johnson & Rossman, 2003]. The density of the sample can be estimated from the general proportion and density of the end members of the mineral phase [Xia et al., 2006]. There is a small thickness variation in each of the samples but it is small (<10%) so the average thickness was taken. An orientation factor of 1/3 was applied to the unpolarised spectra [Paterson, 1982].

Electron microprobe analysis

For accurate and precise chemical compositions of the mineral phases present in the samples we used a JEOL JXA-8530F Hyperprobe Field Emission Electron probe microanalyser in the Electron Microscopy facility at Utrecht University with an acceleration of 15 kV. Two carbon coated thin sections were analysed. Backscattered electron imaging was used to differentiate between the different phases, EDX was used for quick spot analyses to determine the phases, and wavelength-dispersive spectrometry (WDS) was used to get more precise spot analyses.
The positions of the WDS spot analyses were determined by analysing previous SEM maps of thin sections previously measured. Areas of interest were highlighted on these maps making them easier to find during the session. WDS spot analyses were taken on the core and rims of relevant mineral phases to determine if there is a chemical variation between the core and rims as well as between the same mineral phases.

Geothermometry

For one San Quintin lower crustal xenolith the equilibrium temperature was determined by applying two different calibrations of the two-pyroxene geothermometers. [Brey & Köhler, 1990; Taylor, 1998]. We also used the calsium in orthopyroxene geothermometer by Brey & Köhler [1990], and the aluminium and chrome in orthopyroxene geothermometer by Witt-Eickschen & Seck, [1991]. The temperatures were estimated at an assumed pressure of 8 kbar, which is roughly at the moho depth. Although the extraction depth of the xenoliths is uncertain the effect of pressure on calculated two-pyroxene temperatures is 2 °C/kbar.

Results

Rock samples

The xenoliths used for this research have diameters that range from about 2 to 15 cm. One upper mantle xenolith and twenty-four lower crustal xenoliths were studied.
From macroscopic observation the lower crust xenoliths seem to consist predominantly of clinopyroxene and plagioclase. The xenoliths can therefore be described as gabbros and granulites. One of the lower crust xenoliths (SQ16) contains olivine in addition to plagioclase and clinopyroxene. Olivine in the xenolith is partly serpentinized. Lower crustal xenoliths can show both a massive structure and a banded structure. The banded structure alternates between clinopyroxene aggregates and plagioclase aggregates (figure 12). The xenoliths with the banded structure (figure 12A-B) are more common than the xenoliths with the massive structure (figure 12C-D).
The xenolith of the upper mantle called SQ-68 (figure 13) is strongly foliated with macroscopically visible elongated minerals. Olivine is the most abundant phase in this sample and makes up the matrix. The elongated darker green mineral is clinopyroxene and the thin darker streaks are spinel or orthopyroxene. The dark grains that are much less stretched are orthopyroxene. The alignment of orthopyroxene and spinel produces the well-developed foliation and lineation in the xenolith.

Composition

Petrographic characterization of the xenoliths using light microscopy

Table 1 shows the mineral phase and percentage, rock type and general microstructure of all the studied xenoliths. Mineral phases present in the upper mantle xenolith have already been mentioned in the rock type section and figure 7. Olivine takes up most of the sample at around 70%, clinopyroxene is often concentrated in aggregates comprising only a small part of the rock (~10%), orthopyroxene is mostly present as large porphyroclasts (~15%) and spinel is only present as randomly distributed grains (~5%). The deformed lower crustal samples consist almost entirely of plagioclase (40-60%) and clinopyroxene (40-60%) at a relative even ratio. Four of the deformed samples (SQ-16, SQW-22, SQW-75, and SQW-114) have a small amount of orthopyroxene (1-5%). Spinel is present in five samples (SQ-16, SQW-70, SQW-75, SQW-110, and SQW-114) in varying amount that usually range between 1-5% but could reach 20% in SQW-114. Spinel is green in ppl in all the lower crustal xenoliths and is found either at clinopyroxene grain boundaries or as inclusion. Almost all the deformed samples have a low amount (1-5%) of opaque mineral(s), usually along pyroxene boundaries. SQW-75, SQW-110 and SQW-115 contain some very small olivine grains in the reaction rims or melt intrusions (figure 11) that take up very little of the sample (up to 2%). SQ-16 has a significant amount (~5%) of olivine relative to other lower crustal samples concentrated in aggregates (figure 6). SQW-76 has a composition that is not comparable with the other samples. It has a high amount of plagioclase (~70%), a significant amount of opaque a mineral(s) (~20%) and a relative low amount of clinopyroxene (~10%). The igneous samples either have a high abundance of plagioclase (~80%) with an unidentified second phase or a high amount of pyroxene (~60% cpx, 10% opx) and relative little plagioclase (~30%).

Microstructures

Microstructures in the mantle xenolith

The thin section of the mantle xenolith shows a porphyroclastic microstructure (figure 14). Olivine, spinel and some of the orthopyroxene porphyroclasts are elongated and their alignment define a well-developed foliation that can also be observed in hand specimen scale (figure 13). The xenolith predominantly consists of fine grained olivine grains, which surround larger olivine grains (figure 14 A-B).

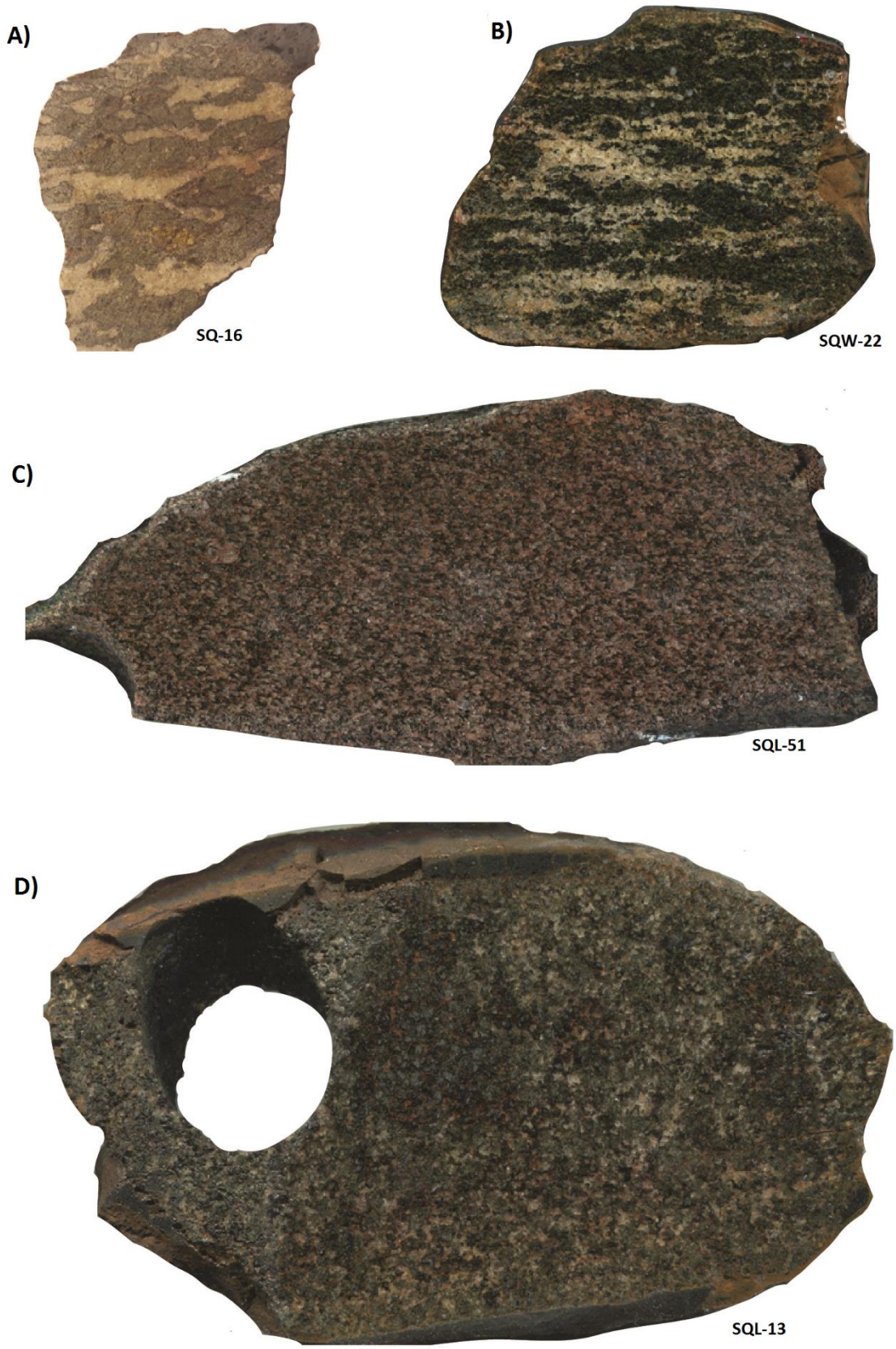

Figure 12: Lower crustal xenoliths collected from the two northen San Quintin Volcanoes. A) Sample SQ-16 shows a banded structure that is divided by plagioclase and clinpyroxene aggregates. In this sample there are also some olivine aggregates. B) Sample SQW-22 shows a similar banded structure as SQ-16 but there is no olivine present on a macroscopic scale. C) Sample SQL-51 has a more granular structure. The plagioclase and clinopyroxene grains are of the same size and appear to be uniformly distributed in the rock. D) Sample SQL-13 also shows a granular structure but contains a higher volume of pyroxene and the grain size appear larger.

Figure 13: Upper mantle sample SQ-68. The sample shows clear signs of deformation through the weak compositional banding and the elongated minerals. The light green minerals that occupy a large part of the rock as the matrix are olivine. The darker green bands that seen through the xenolith as clinopyroxenes. The almost black minerals that can be elongated are orthopyroxenes.

Some of the olivine porphyroclasts show undulose extinction but all the recrystallized olivine grains and the majority of the olivine porphyroclasts show a flat extinction. Furthermore, olivine-olivine grain boundaries may show 120° triple junctions. Many of the grains surrounding the orthopyroxene porphyroclasts show curved/concaved boundaries. Clinopyroxene is found as small grains inside the olivine matrix or as aggregates. Clinopyroxene grains are generally not elongated except when bordering orthopyroxene porphyroclasts, showing elongation perpendicular to the foliation (figure 14C-D). The orthopyroxene porphyroclasts contain exsolution lamellae, which tend to align with the foliation. The orthopyroxene porphyroclasts show intragrain deformation evidenced by kinked exsolution lamellae and undulose extinction (figure 14D). The sample has a strong CPO when viewed through a gypsum plate.

Microstructures in the lower crustal xenoliths

Not all the lower crustal xenoliths show microstructural evidence of deformation. Seven of the lower crustal xenoliths (SQL-12A, SQL-13, SQL-17A, SQL-47A,B & C, SQL-100, SQW-81, SQW-88, and SQW-95) display an igneous microstructure affected by only limited deformation. On a macroscale these xenoliths have a granular or massive structure. Four of the xenoliths with the igneous microstructure contain a very high amount of pyroxene compared to plagioclase, whereas two lower crustal xenoliths (as in figure 15) only have feldspars. In the first case (SQL-12A, SQL-13, SQL-17A, SQL-100) the pyroxene grains are included into very large plagioclase grains. Pyroxene grains in these samples have exsolution lamellae and may have rounded inclusions, which are most likely cumulative structures. The plagioclase grains have abundant growth twins. The size of the plagioclase grains is hard to determine because the pyroxenes overlap most of them but it is estimated to be between 1 and 5 mm. In the igneous lower crustal samples with only feldspar, large plagioclase grains containing mechanical twinning take up most of the sample. These grains are often intruded by a new phase that is hard to identify. The unknown phase shows microstructures that can be related to igneous processes. Figure 15

shows an example of such an igneous microstructure for a xenolith containing mostly plagioclase. The plagioclase grains in these samples are between 1-3 mm in size.

Table 1: information regarding identified mineral phases, rock type and microstructure texture for each studied sample.

Samples	Mineral phases	Rock type	Microstructure
SQ-68	Ol (70%), cpx (10%), opx (15%), sp (5%)	Iherzolite	Porphyroclastic
SQ-16	Plg (41%), cpx (42%) opx (5%), sp (2%), ol (5%)	Granulite	Granoblastic
SQL-48	Plg (47%), cpx (47%), opq (6%)	Granulite	Granoblastic
SQW-78	Plg (40%), cpx (47%), opq (3%)	Granulite	Granoblastic
SQW-110	Plg (55%), cpx (40%), opq (5%)	Granulite	Granoblastic
SQL-51	Plg (40%), cpx (40%), opq (20%)	Granulite	Granoblastic
SQW-79	Plg (40%), cpx (55%), opq (5%)	Granulite	Granoblastic
SQW-114	Plg (10%), cpx (40%), opx (30%), spl (20%)	Granulite	Granoblastic
SQW-70	Plg (45 %), cpx (40%), melt (15%)	Granulite	Granoblastic
SQW-75	Plg (50%), cpx (40%), opx (5%), spl (3%), Ol (2%)	Granulite	Granoblastic
SQW-200	Plg (40%), cpx (47%), opq (3%)	Granulite	Granoblastic
SQW-95	-	Basalt	Igneous
SQW-88	Plg (80%), Unknown (20%)	Gabbro	Igneous
SQW-81	Plg (80%), Unknown (20%)	Gabbro	Igneous
SQW-22	Plg (45%), cpx (50%), Spl (5%)	Granulite	Granoblastic
SQL-47 (A,B,C)	Plg (30%), cpx (65%), opx (15%)	Gabbro	Igenous
SQL-100	Plg (30%), cpx (65%), opx (15%)	Gabbro	Igenous
SQL-13	Plg (30%), cpx (65%), opx (15%)	Gabbro	Igneous
SQL-12A	Plg (30%), cpx (65%), opx (15%)	Gabbro	Igneous
SQW-115	Plg (47%), cpx (47%), opq (6%)	Granulite	Granoblastic
SQL-58	Plg (30%), cpx (65%), opx (15%)	Gabbro	Igneous
SQW-80	Plg (40%), cpx (40%, melt (20%)	Granulite	Granoblastic
SQL-17A	Plg (30%), cpx (65%), opx (15%)	Gabbro	Igenous
SQL-54	Plg (40%), cpx (40%), opq (20%)	Granulite	Granoblastic
SQW-76	Plg (80%), qrtz (5%), opq (15%)	Granulite	Granoblastic
SQW-83	-	-	-

The deformed lower crustal xenoliths have similar microstructures to each other. The most common microstructures are shown in figure 10. Interlobate boundaries are found for both plagioclase and pyroxene grains in nearly all the samples (SQ16, SQL-48, SQL-51, SQW-22, SQW-75, SQW-76, SQW-78(1&2), SQW-79, SQW-80, SQW-110, SQW-114, and SQW-115). However, pyroxene-plagioclase boundaries are usually less irregular (figure 16A-B). In addition to the interlobate boundaries some boundaries also show bulging (figure 16B). Most plagioclase grains in the samples exhibit mechanical twinning but some grains have growth twinning as well. Figure 16D shows an example of both deformation twinning (twins that are irregular and sometimes discontinuous) and growth twinning (twins are straight and parallel). There are some samples however that only have plagioclase with growth twinning (SQW-70, SQW-78(2) and SQW-114). The plagioclase grains in these samples are always close to melt intrusions. Plagioclase and pyroxene grain sizes seem variable all the deformed samples. It is not very uncommon for plagioclase to have subgrains. Pyroxene grains often show a bimodal grain size distribution where "fresh" recrystallized grains surround a relic porphyroclast. These old relic grains often have exsolution lamallae that sometimes run parallel to the foliation (figure 16 C-D). Basaltic intrusions are present in four xenoliths (SQL-48, SQW-70, SQW-78(2), and SQW-80) that make dark blobs in random locations throughout the sections. Other samples (SQ-16, SQW-75, SQW-110, and SQW-115) have either a reaction rim between pyroxene grains and plagioclase or an earlier melt

intrusion which was deformed along with the grains (figure 17). The thin section of sample SQW-22 shows plagioclase grains with undulose extinction. But these grains are rare and distributed randomly through the sample. All the other xenoliths show grains with a flat extinction. The deformed lower crustal xenoliths show a strong CPO, when inspected through a gypsum plate (figure 18A-B),

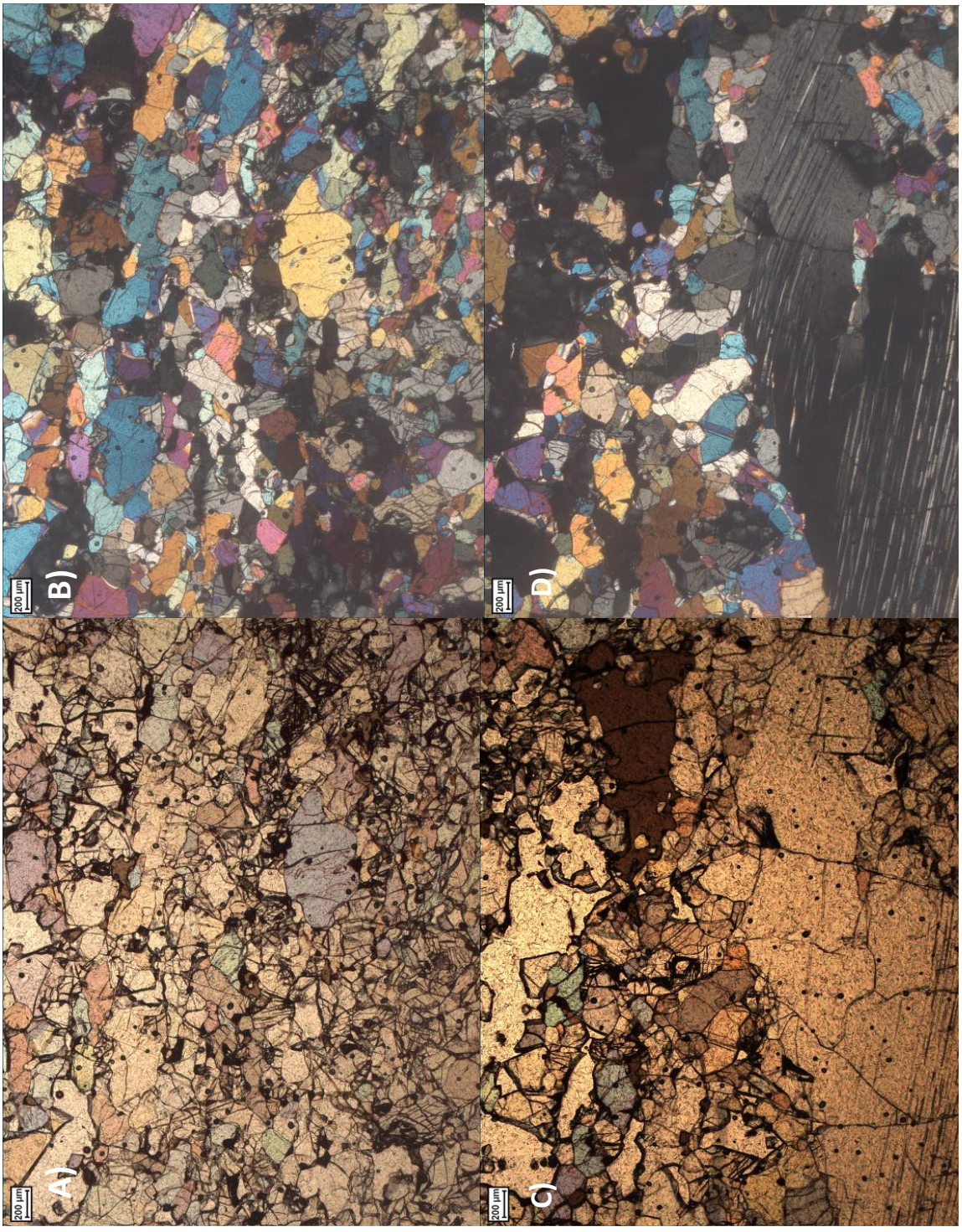

Figure 14: Plain polarized and cross polarized light micrographs of the upper mantle sample (SQ68). The The xenolith is characterized by a well-developed foliation, defined by the elongation and alignment of olivine, spinel, and orthopyoxene grains. The foliation is left-right horizontal on all the micrographs. A-B) Bands of Larger elongated olivine grains are surrounded by smaller elongated olivine grains which highlight the foliation. Although the extinction of most olivine grains is flat some larger olivine grains have an undulose extinction. Spinels are distributed throughout the sample and show an elongation parallel to that of the olivine. Small pyroxene grains are present in clusters or as a single grain and show almost no preferred orientation. C-D) Large orthopyroxene porphyroclasts are present throughout the sample. These porphyroclasts are often elongated parallel to the foliation, show undulose extinction, and contain exsolution that is sometimes kinked. Pyroxene grains surrounding the large porphyroclasts often appear elongated perpendicular to the foliation.

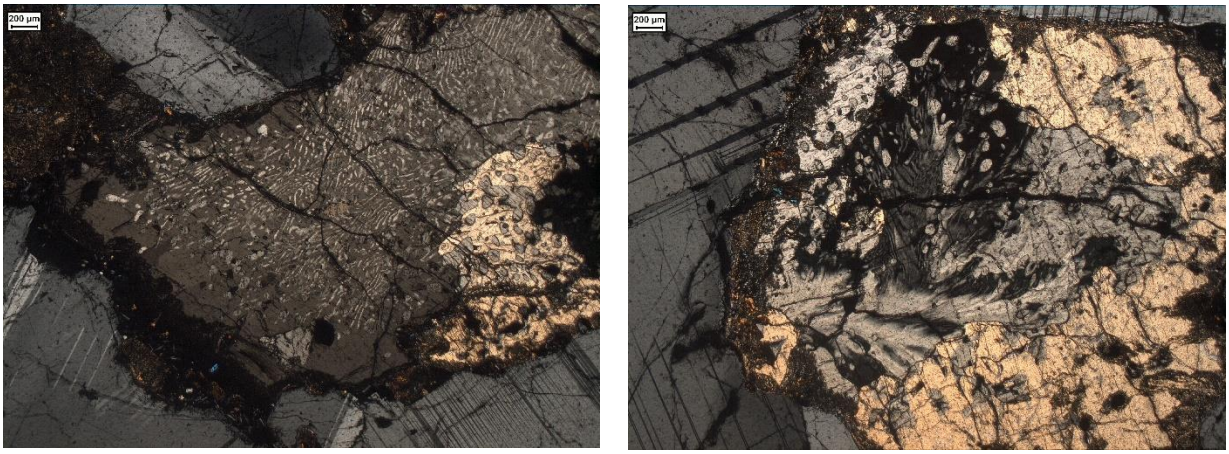

Figure 15: Xpl micrographs of sample SQW-88. The microstructure of this sample displays a clear influence of melt. The left micrograph shows worm-like inclusions of an unknown phase in the grey-brownish feldspar while the light brown patch on the right part of the photomicrograph shows more rounded inclusions. The right micrograph also contains the rounded inclusions in the lighter brown feldspar patch and shows a fibrous flow structure. The large plagioclase grains that are next to these structures do include mechanical twinning.

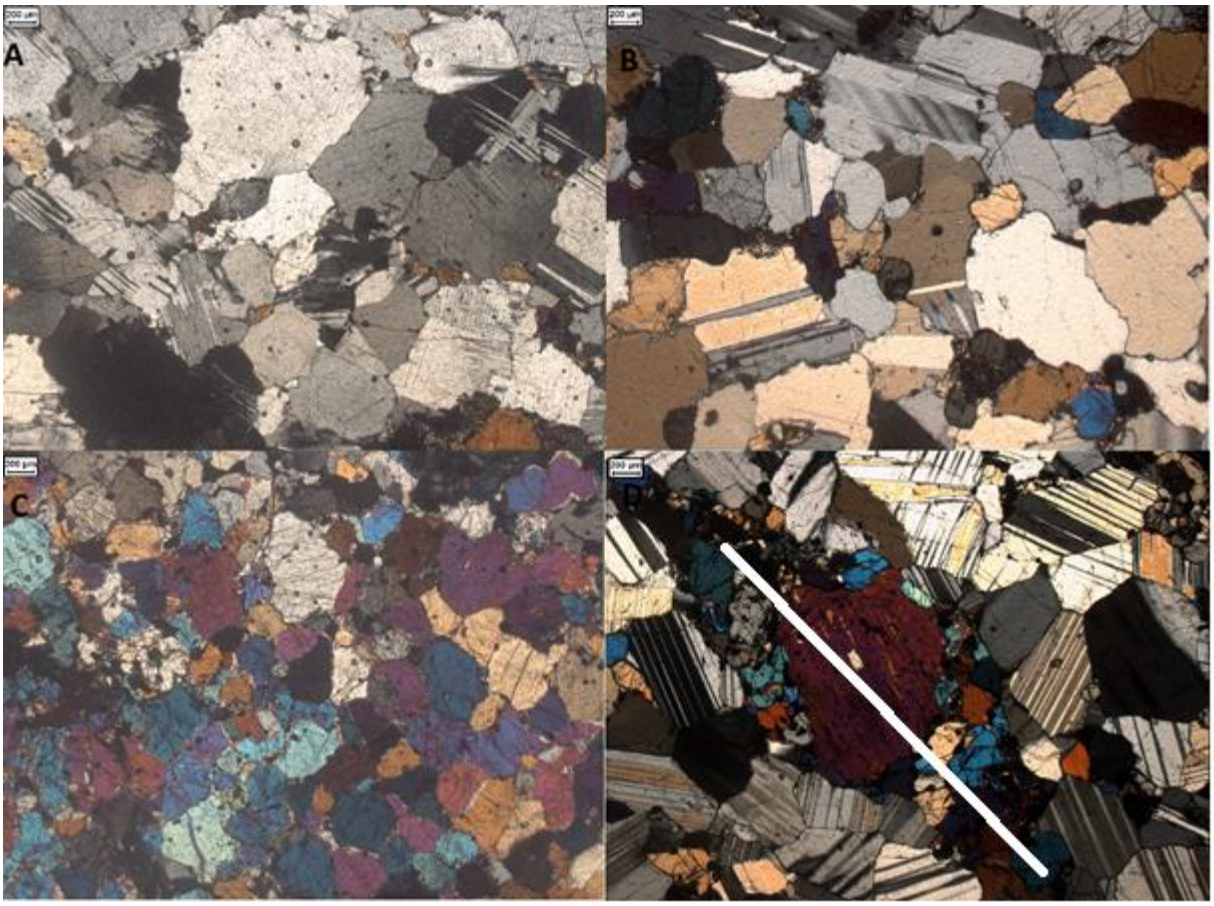

Figure 16: Cross polarized micrographs of common microstructures in the lower crustal xenoliths. A) Sample SQ-16 shows plagioclase grains with variable sizes that have irregular or interlobate boundaries. Grain sizes are variable in this sample showing a bimodal distribution. Mechanical twinning is present in most plagioclase grains regardless of their size. B) Sample SQW-78(1) has a very similar microstructure to that of SQ-16. The grain boundaries in this sample are even more interlobate and some boundaries seem to bulge in to the neighbouring grains. Mechanical twinning is common in the plagioclase grains and foliation is hard to decipher in the microscale. C) The pyroxene grains in SQ-16 also have interlobate boundaries but they are less pronounced as they are in plagioclase in the same sample. Some larger pyroxene grains show more internal deformation and have exsolution. D) Sample SQW-75 contains clinopyroxene aggregates that show the direction of the foliation. The direction of the foliation is indicated with a white line.

although CPO may weaken or become random in xenoliths with basaltic material between the pyroxene and plagioclase grains (figure 18C-D). Sample SQW-75 has a significant amount of plagioclase grain boundaries that make triple junctions with angles of 120° with each other. These triple junctions can be found for pyroxene as well in the sample but are less often (figure 19).

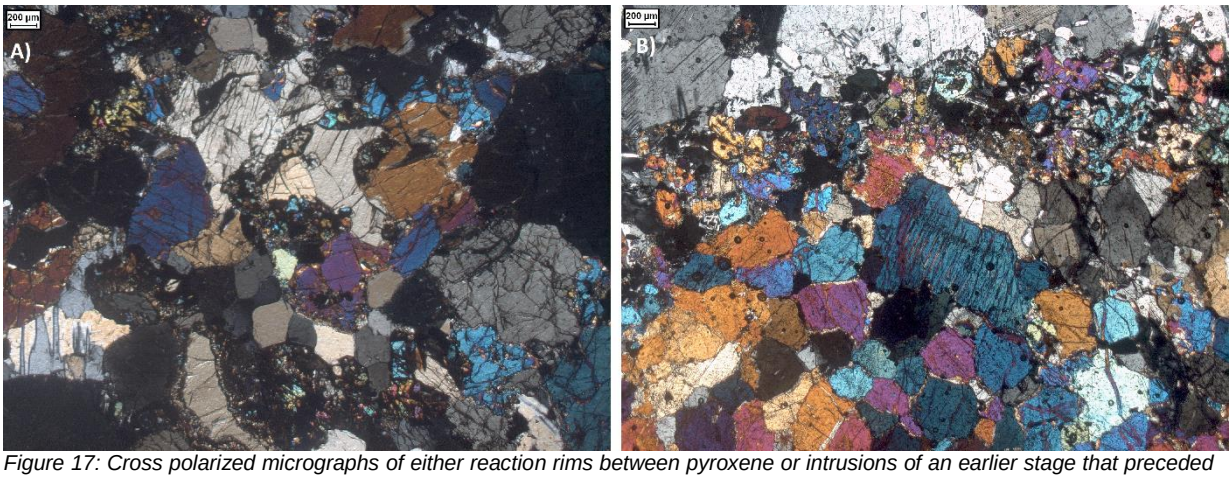

Figure 17: Cross polarized micrographs of either reaction rims between pyroxene or intrusions of an earlier stage that preceded deformation. A) SQW-115 has large dark batches of melt that surround pyroxene or lay between plagioclase and pyroxene. B) SQ-16 has large bands of either an alteration product of a melt intrusion between the plagioclase and pyroxene aggregates.

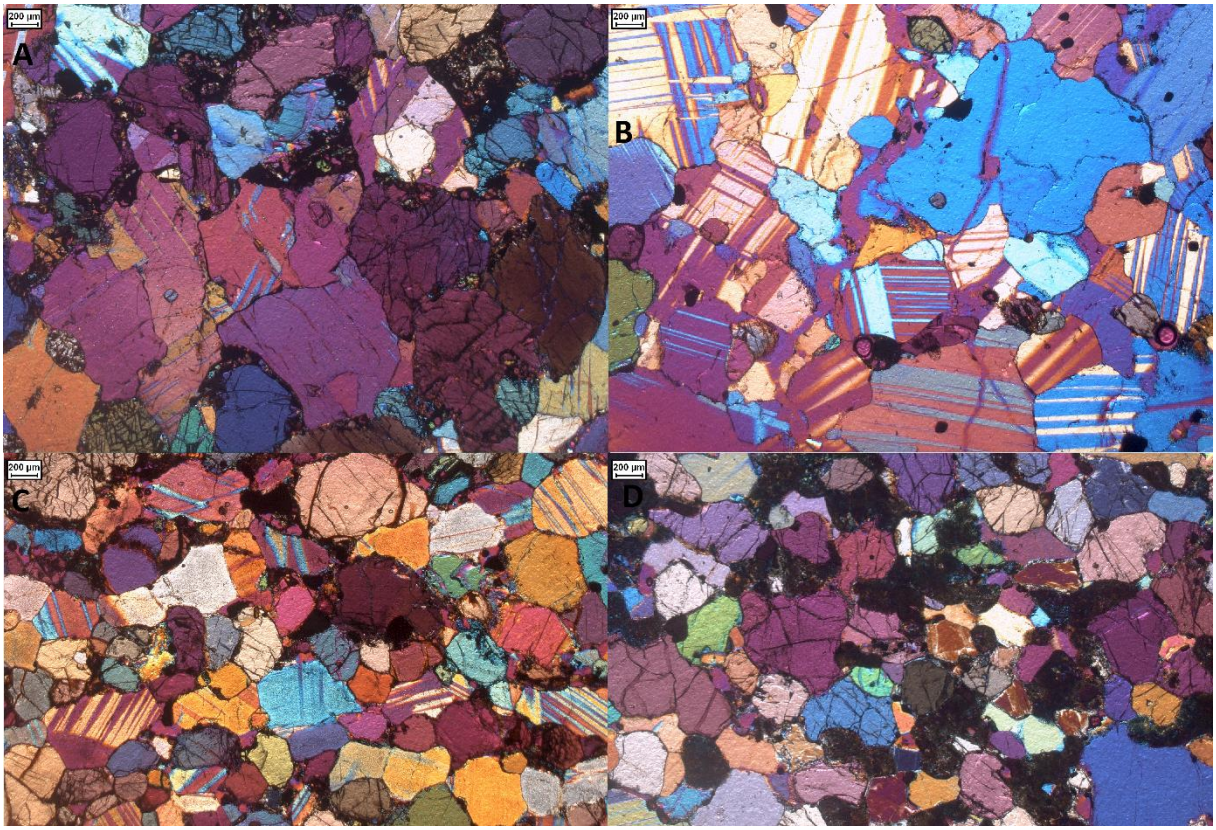

Figure 18: Photomicrographs of the crystallographic orientations of pyroxene and plagioclase grains in the deformed lower crustal xenoliths. A) SQW-115 shows one big cluster of different plagioclase grains with similar orientations. B) SQW-110 shows at least two plagioclase clusters of grains with similar orientations. C) SQL-48 shows random CPO of both plagioclase and pyroxene grains. D) SQW-80 shows a weaker CPO compared to SQW-115 and SQW-110.

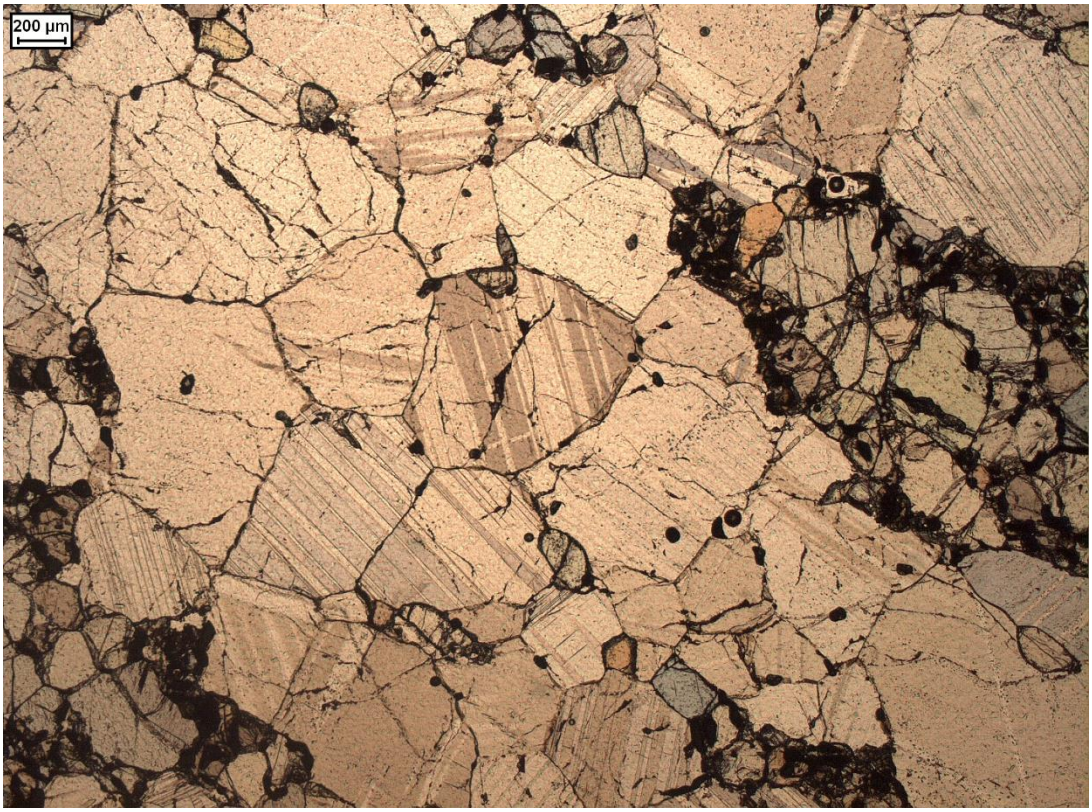

Figure 19: Ppl photomicrograph of SQW-75. The plagioclase grain boundaries often from triple junctions with angles of 120° producing a foam (or polygon) like microstructure. Pyroxene grains in this sample also show some of these triple junctions but less often.

Scanning Electron Microscopy analysis

To determine the mineral compositions of the lower crustal xenoliths, four samples were analysed by Scanning Electron Microscopy (SEM). SQ-16, SQW-75, and SQW-114 were selected as representative of the deformed xenoliths. SQW-76 was selected because its composition was different from all the other deformed samples.

SQ-16

Figures 20 to 22 show some of the spot analyses carried out in the xenolith. The z-contrast images in figure 20 give a good representation of what the bulk composition looks like. There are the two major phases, plagioclase and clinopyroxene, that only have a small density contrast with each other. Figure 20 shows the boundary between these two phases. The brighter phase on the right of the z-contrast images is clinopyroxene. The composition of clinopyroxene generally shows the presence of magnesium and a slight amount of iron and can therefore be considered as mostly diopside ($MgCaSi_2O_6$) that forms a solid solution with a small percentage of hedenbergite (FeCaSi2O6) and or augite ($(Ca,Na)(Mg,Fe^{2+},Al,Fe^{3+},Ti)[(Si,Al)_2O_6$) to account for the Al and Fe. The darker phase on the left is plagioclase. The composition of plagioclase seems to be purely anorthite (CaAl2Si2O8) as no Na is present in the plagioclase grains.
Figure 20 also shows some very bright spots in the boundary and near the edges of the clinopyroxene and plagioclase grains. This bright phase can be found throughout the sample and a spot analysis has been made of it on the left image in figure 21. The analysis shows that this phase is an iron oxide. Figure 21 and 22 are z-contrast images of the bands that can be found in between plagioclase and pyroxene aggregates. The z-contrast image shows patches of four different phases intertwined with each other. The spectroscopy graphs of the spot analysis of figure 21B and in figure 22A are almost identical to the graphs of figure 20 which represent plagioclase. The only difference is that there is Na present figure

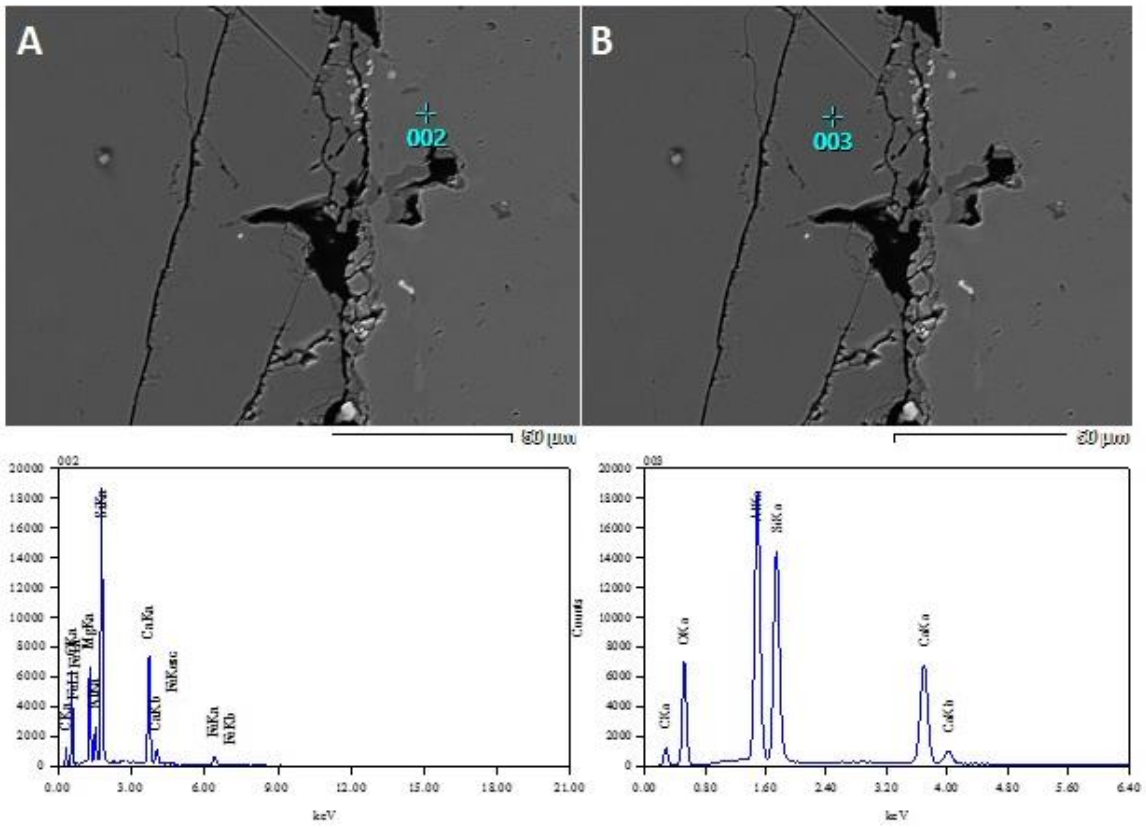

Figure 20: The top images are Z-contrast images of the two major phases in the sample (plagioclase and clinopyroxene). Between the two phases there are some small grains of a heavier mineral. A) The clinopyroxene composition has been measured at spot 002 and shows a higher amount of Mg relative to Fe. B) Plagioclase composition has been measured at spot 003. The plagioclase seems to have no Na.

22A. The EDX spot analysis of the top right in figure 16 is a new phase however and shows a high count of magnesium that matches the silica count and a moderate amount of Fe, making it olivine.
Figure 23 shows an element overlay map for a z-contrast image of the patchy band similar to that of figure 21 and 22 to see if there is any noticeable exchange of elements between phases. The overlay map of figure 24 shows a patchy sequence of different phases that match the boundaries of the phases of the Z-contrast image perfectly and therefore provide no evidence for elements exchange between the phases. In addition to the elements shown in the overlay map the blobs indicated by 1b in figure 23 also contain sulphur.
The microstructure of the sample in BSE images is very monotone. The plagioclase and clinopyroxene aggregates take up most of the sample and there is very little deviation of z-contrast in these aggregates (figure 20). The bands between the aggregates have a very patchy structure (figure 21, 22 and 23).

SQW-75

The general composition of the plagioclase grains in the xenolith is shown in figure 24A. As in sample SQ-16 the plagioclase seems to be purely anorthite. A trace amount of Na might be present but it does not show up on the SEM spectra. The clinopyroxene composition is shown in figure 24B, and similar to SQ-16 clinopyroxene consisting mostly of diopside with a small percentage of hedenbergite and/or ugite. The exsolution that is present in some of the larger clinopyroxene grains is spinel with a high chrome content (figure 25). The spinel exsolution spectra contains some Si which should not be in there. This has likely something to do with the beam width of the table top SEM. The xenolith also contains pockets with complex compositions including: 1) plagioclase, that is mostly anorthite but with a small percentage of albite; 2) clinopyroxene with a composition identical to the major phase clinopyroxene; 3) olivine with plagioclase rims; 4) orthopyroxene; and 5) spinel. Figure 26 shows an element map taken

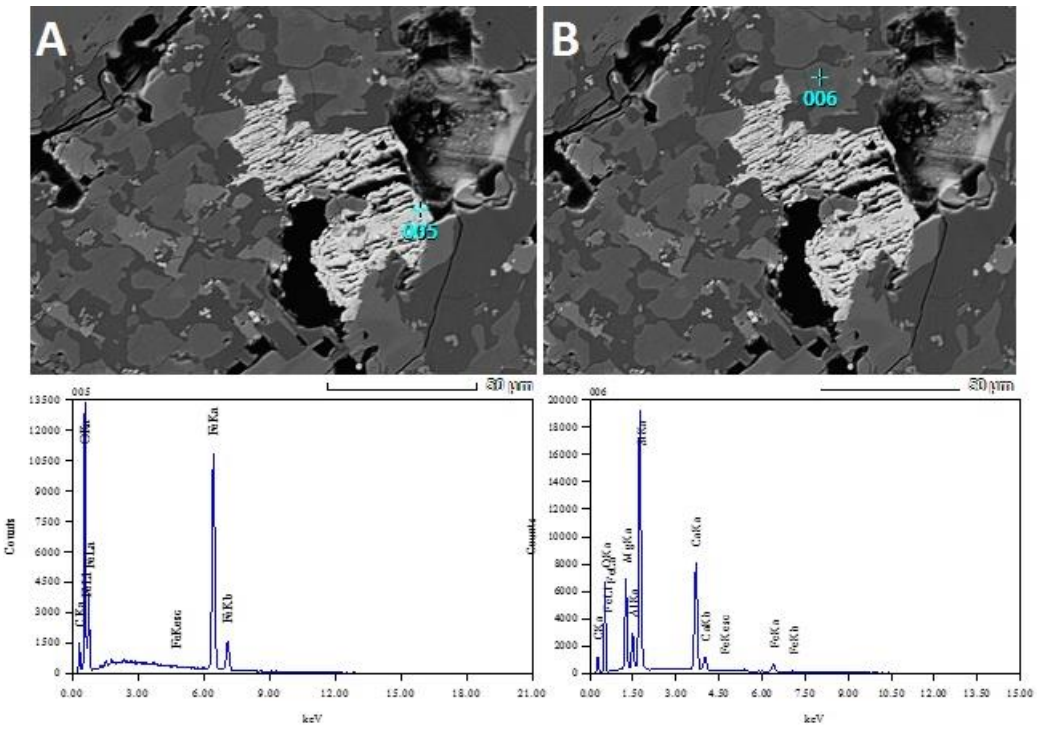

Figure 21: Z-contrast image taken from the reaction or melt band in between clinopyroxene and plagioclase aggregates. Four different phases can be distinguished in this band. A) Spot 005 is placed on top of the heaviest phase which an iron oxide. C) The phase of spot 006 is clinopyroxene with a composition near identical to that of spot 002 in figure 20.

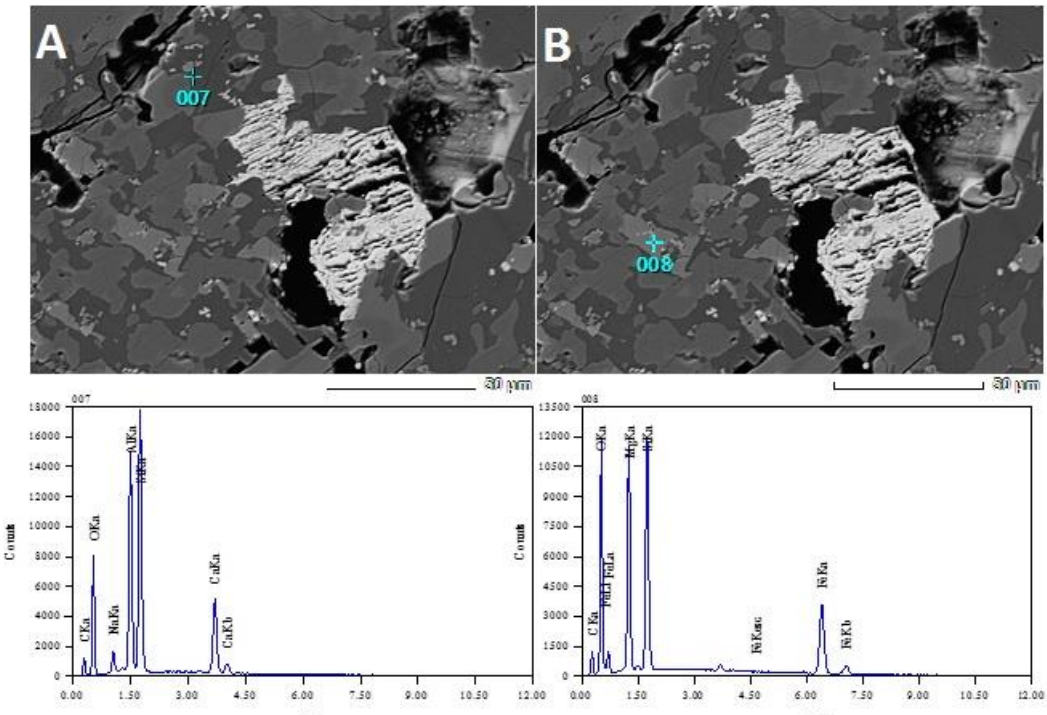

Figure 22: The measurement of the last two phases in the band between pyroxene and plagioclase aggregates. A) Spot 007 is plagioclase with a composition similar to that of spot 003 (figure 20B) but with a significant amount of Na present. B) The last phase has been measured at spot 008 and shows the composition of an olivine.

for one of these patches. The composition of the patches in xenolith SQW-75 is very alike to the bands in xenolith SQ-16.

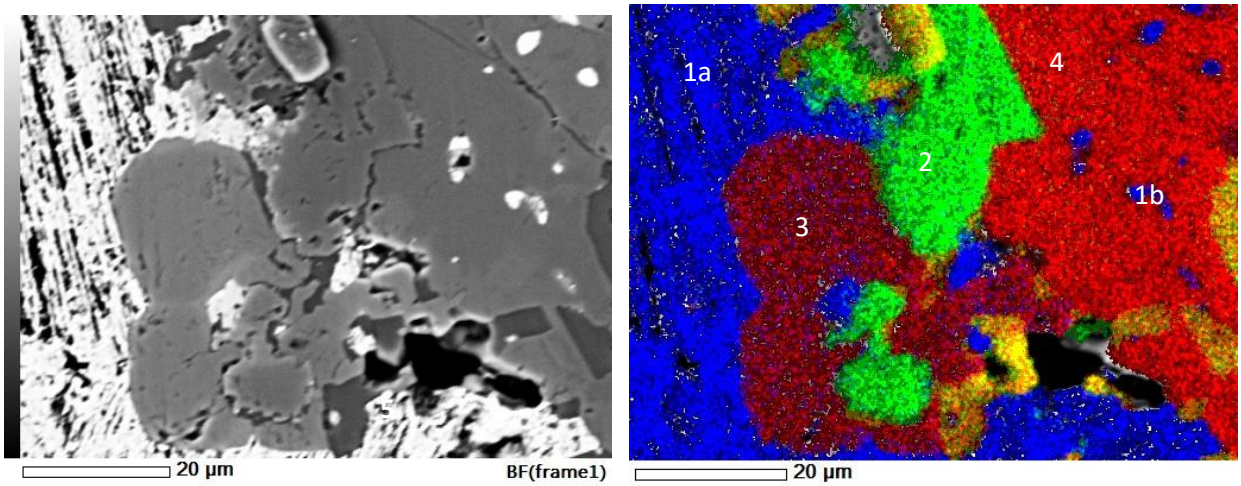

Figure 23: On the left an EDX showing Z-contrast. On the right an element overlay: Si (red), Al (green), Fe (blue). The black spot in the lower right corner is supposed to be a hole in the sample. Phase 1 is an iron oxide with the small spots as 1b presumably being iron oxide melt inclusions. Phase 2 is an aluminium and magnesium oxide containing no silica at all. Phase 3 is supposed to be olivine. Phase 4 is clinopyroxene and phase 5 is an aluminium silicate.

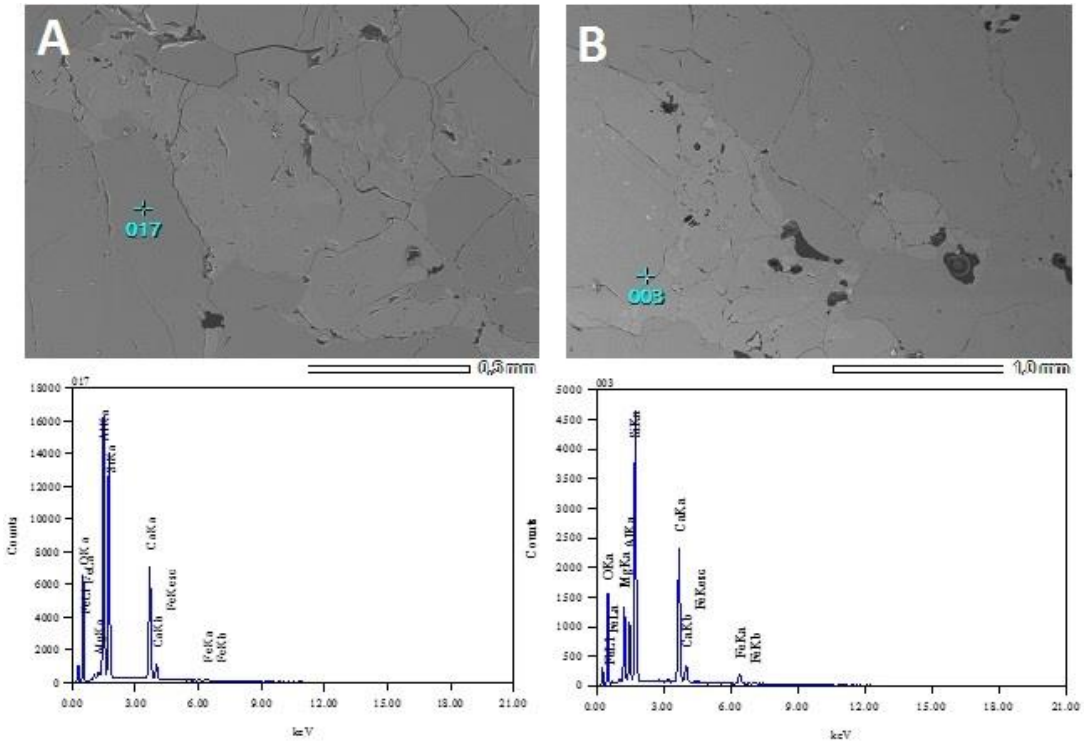

Figure 24: Compositions of plagioclase and clinopyroxene in SQW-75. A) Spot 017 is a representative composition of the plagioclase grains in this sample, relatively large amount of Ca and no Na. B) Spot 003 gives the general composition of clinopyroxene with a high abundance of Ca and a low amount of Fe.

The BSE images show a texture similar to that of SQ-16 where the major phases are very monotone and show little variation in z-contrast. Only the patches or bands that are present through the sample show random patches of grains.

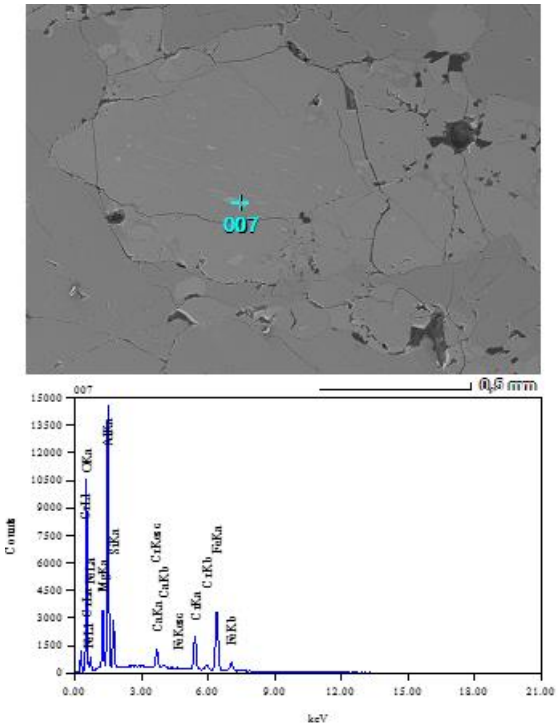

Figure 25: Spot analysis of the exsolution in a clinopyroxene grain present in sample SQW-75. The composition belongs to spinel with a high Cr content. Si does not belong in the composition of spinel and is likely measured from the surroundings.

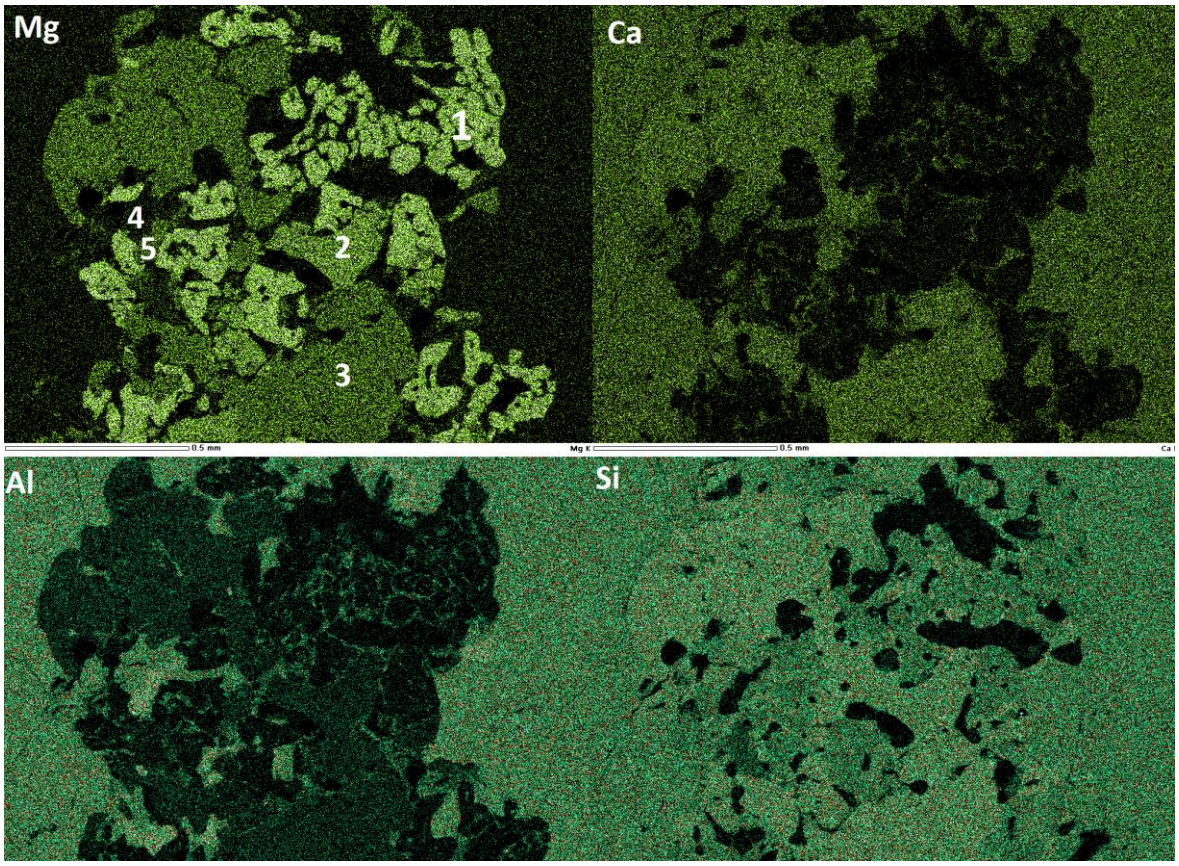

Figure 26: x-ray map of one of the batches that are present in sample SQW-75. The mapped elements are shown in the left upper corner of the images. Mineral 1 is olivine, mineral 2 is orthopyroxene, mineral 3 if clinopyroxene, mineral 4 is plagioclase and mineral 5 is spinel.

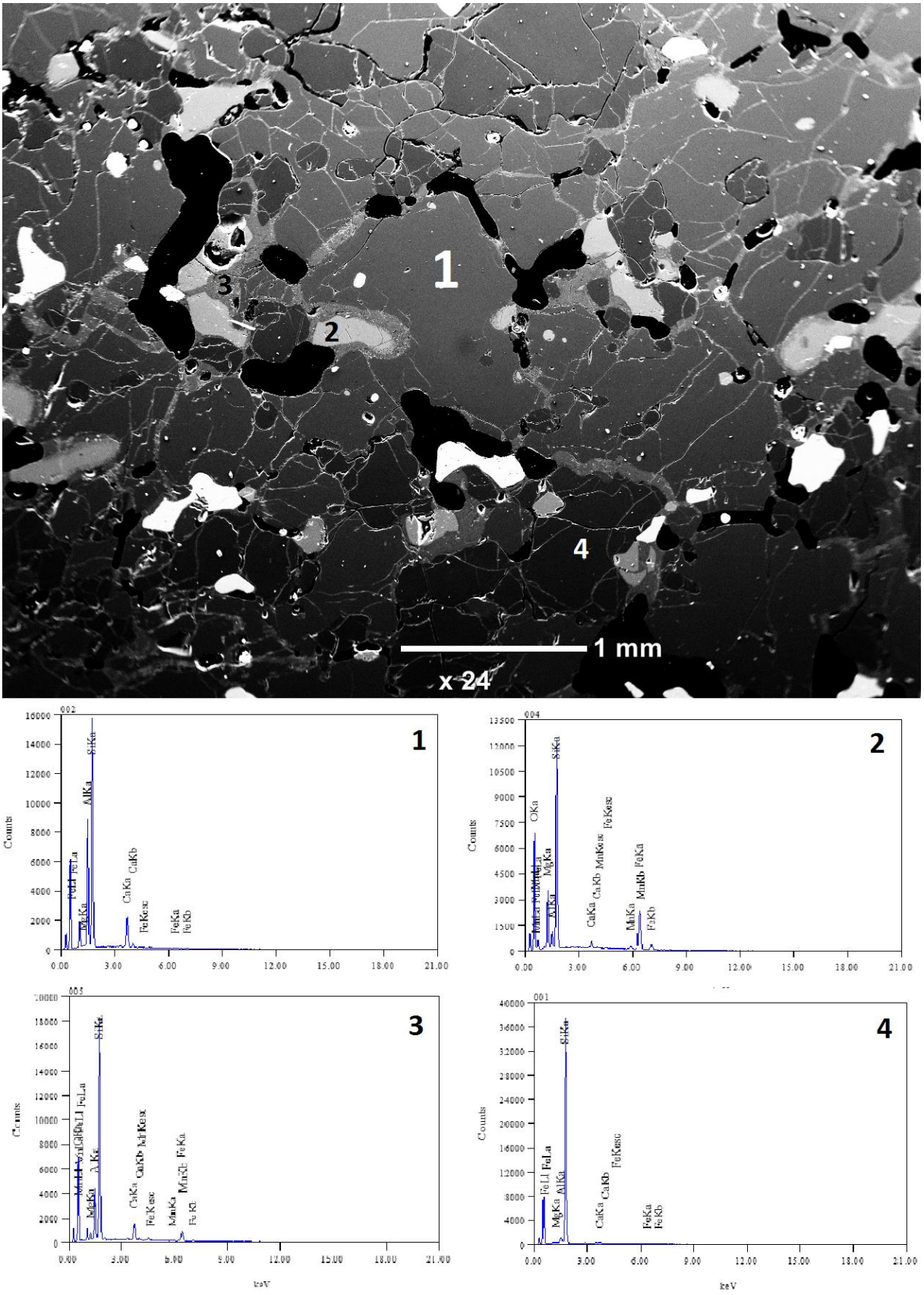

Figure 27: SEM analysis of sample SQW-76. The major mineral phase, which is plagioclase has been marked as 1 in the BSE image. Plagioclase has only little Ca and relatively more Na compared to the other analysed xenoliths. Mineral phase 2 is clinopyroxene with almost an even ratio between Mg and Fe. Mineral phase 3 marks what appears to be an alteration product of clinopyroxene with more Si added. Mineral phase 4 is quartz with significant amount of silica.

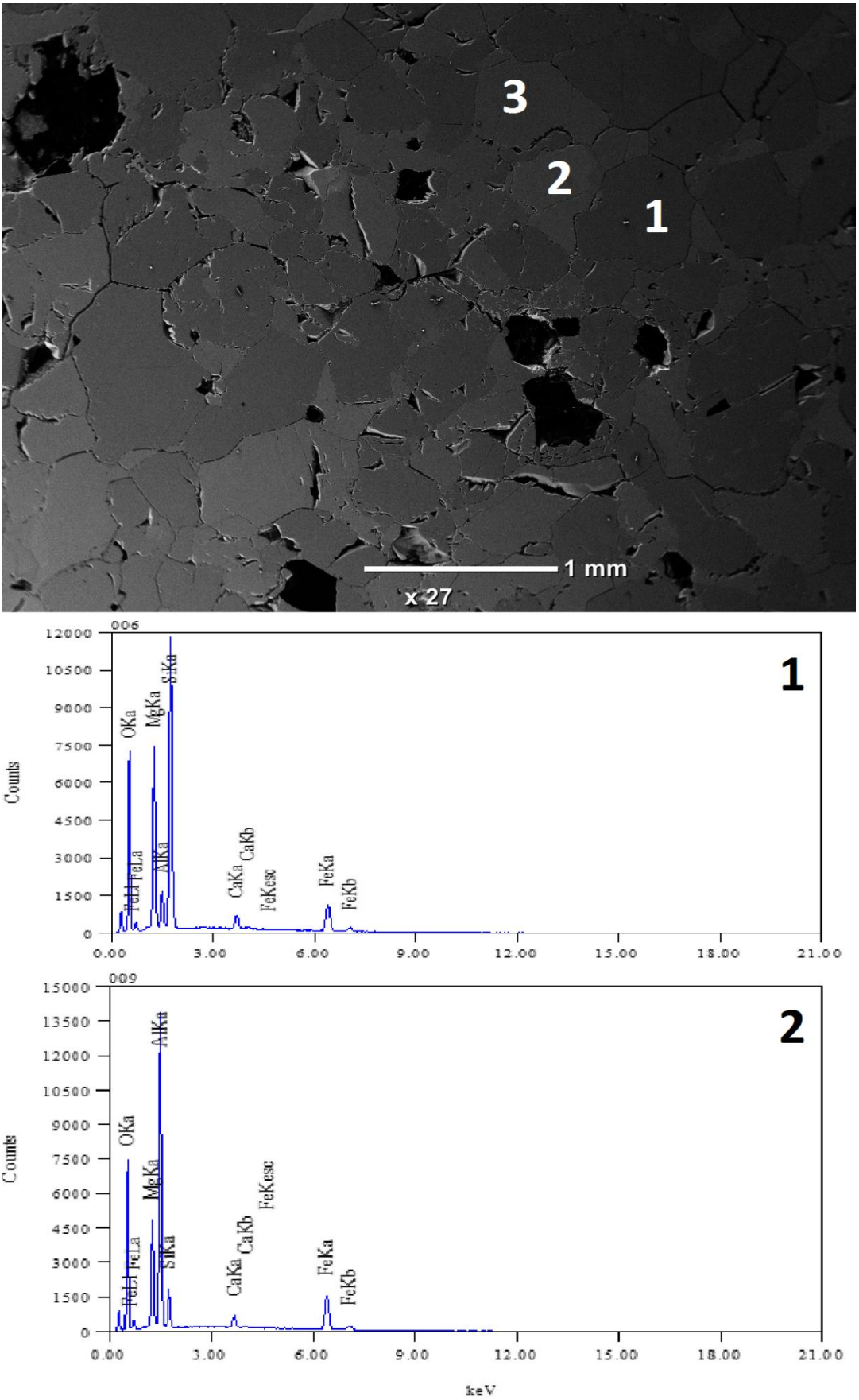

Figure 28: Z-contrast image of SQW-114. The numbers represent the different phases in this image. Phase 1 is orthopyroxene but with a small content of Al and Ca. Phase 2 is spinel with a small Ca and Si content. Phase 3 is clinopyroxene with a composition identical to clinopyroxene in SQ-16.

SQW-76

The composition of this sample is very different from the other deformed samples. Figure 27 shows the general microstructure of the xenolith and the spot analyses carried out for each phase. Plagioclase is the major phase in this sample as has been determined before by optical microscopy. The composition of the plagioclase seems to be a mixture of anorthite and albite at an almost even ratio (around 60% an and 40% ab). Clinopyroxene is not as abundant in this sample as it is in other deformed samples. In addition, the composition of clinopyroxene has much more Fe than in the other deformed samples. Along the boundaries of the minerals there seem to be veins that have a composition almost the same as that of the clinopyroxene in the sample but with more silica. The dark grains in figure 27 are quartz with a very high silica content. The composition of the brightest phase in the sample is not shown in figure 27 but the mineral is ilmenite. Silica is likely saturated in this sample which increases the Si content of all the phases.

SQW-114

This sample has compositional layering that alternates from: 1) plagioclase, melt and clinopyroxene, to 2) clinopyroxene with spinel, and finally to 3) only ortho- and clinopyroxene. The composition of clinopyroxene is similar throughout the sample and comparable with the composition of clinopyroxene in samples SQ-16 and SQW-75. The plagioclase is also comparable with that of SQ-16 and SQW-75 in that it is purely anorthite. The general texture of the sample is shown in figure 28 along with the phases in it and the compositions of spinel and orthopyroxene. The composition of the orthopyroxene consists primarily of enstatite but the small contents of Al, Ca and Fe suggest that there might be some overlap with clinopyroxene. Spinel has no Cr in this sample but does again have a small Si peak.

Electron microprobe analysis

BSE images

The BSE detector of the EMP has a much higher resolution than those of the SEM. Figure 29 shows some compositional structures observed at the EMP. The olivine in SQW-75 is zoned and has a higher brightness at the grain edges. Olivine is surrounded by plagioclase that often has a dendritic appearance. In addition the spinels have a ring of iron oxide blobs around them (figure 29a). The exsolution of clinopyroxene in SQW-75 has spinel but orthopyroxene is also presence in the exsolution (figure 29b). Plagioclase in SQ-16 can have straight brighter domains with no difference in their chemical composition (figure 29c), which is likely due to a change in orientation. The clinopyroxene in the reaction of melt bands between the clinopyroxene has chemical zoning (figure 29d).

Temperature estimates

SQ-16 has been analyzed for temperature estimates. This lower crustal xenolith was chosen because it was one of the better samples for grain size measurements. In addition, the SEM analysis showed that it had both clinopyroxene and orthopyroxene and could therefore be used for two-pyroxene geothermotry.
Table 2 shows the ortho- and clinopyroxene analyses that have been used for geothermometry. The temperatures have been estimated using: 1) the mean of the core measurements; 2) the mean of the measurements at the grain rims; or 3) the mean of all the measurements including both cores and rims. Results from these three approaches were compared. The measurements from region 1 were not included in our analysis because their standard deviation was too high for some of the analyzed elements. The calculated temperature from the two-pyroxene geothermometers (Brey & Köhler, 1990; Taylor; 1998) ranges 664 – 776 °C for the cores, 669-735 °C for the boundaries and 692-744 °C for the combination

of cores and boundaries. The calcium in opx and Al&Cr in opx geothermometers give a temperature range of 840-860 °C for all the means.

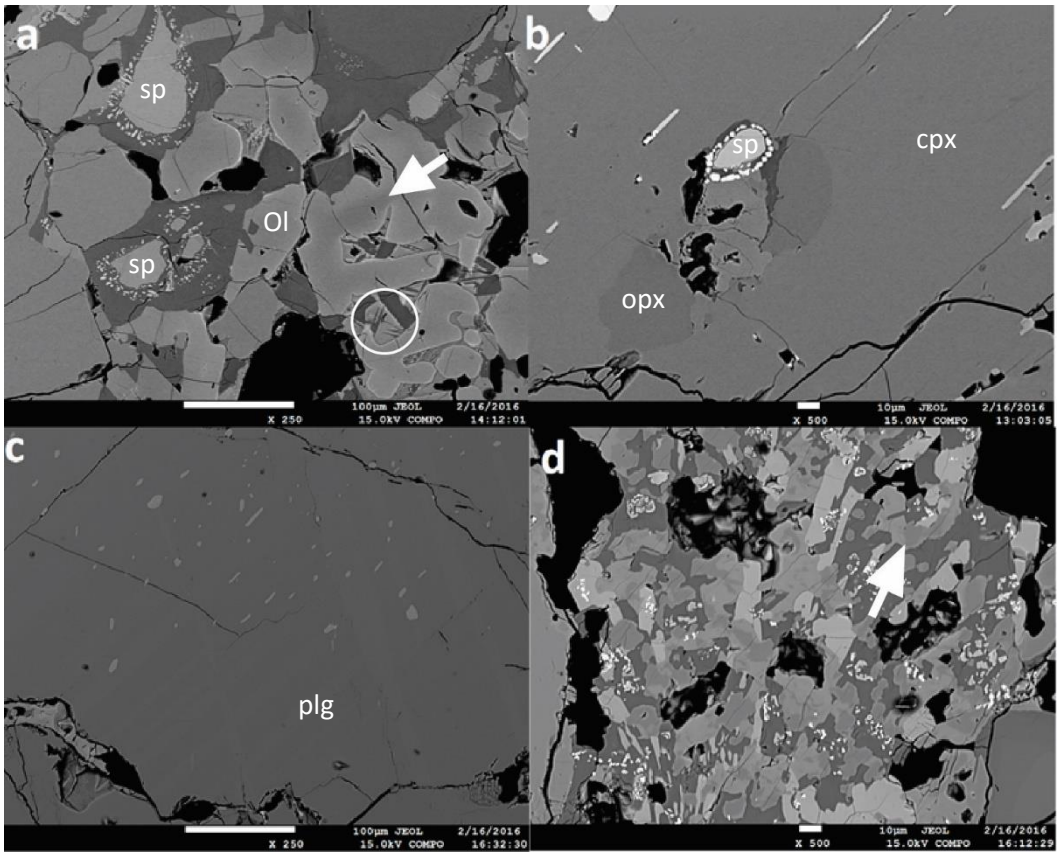

Figure 29: High resolution BSE images made with the EMP. Images a and b are from sample SQW-75 and images c and d are from SQ-16. Image a shows the z-contrast of one of the pockets that contain olivine (Ol) in sample SQW-75. The image shows zoned olivine indicated with an arrow. Olivine is surrounded by plagioclase that shows dendritic forms indicated with a circle. Spinels (sp) in this image are surrounded by iron oxide blobs and plagioclase. b shows the spinel exsolution in clinopyroxene but now it also shows that there is orthopyroxene and plagioclase present in the exsolution as well. In addition the spinel is again surrounded by iron oxide blobs. C shows a aggregate of plagioclase in SQ-16. There are stripes of lighter contrast running through the aggregate. d shows the z-contrast of one of the bands between pyroxene and plagioclase. The image shows the same structure as has been seen before but also shows that clinopyroxene has zoning in these bands, which is indicated with an arrow.

Table 2: Ortho- and clinopyroxene analysis for sample SQ-16

	Orthopyroxene									
	1 c	1 b	2 c1	2 c2	2 b	3 c1	3 c2	3 b	4 e1	4 e2
wt%										
SiO2	51.8	53.11	53.19	53.12	52.95	53.01	53.12	53.61	52.73	52.98
TiO2	0.0221	0.0224	0.0283	0.0136	0.0344	0.0192	0.0433	0.0288	0.0062	0.0315
Al2O3	2.67	3.17	2.4	2.88	2.83	2.95	3.06	2.8	3.12	2.88
Cr2O3	0.1489	0.1705	0.1785	0.1746	0.2153	0.1947	0.217	0.2256	0.2273	0.2149
FeO	16.6	16.47	16.28	16.38	16.53	16.66	16.99	16.41	16.37	16.04
MnO	0.4096	0.3869	0.4064	0.3951	0.4091	0.3912	0.4113	0.3812	0.3761	0.3772
MgO	24.46	26.92	26.27	25.99	25.93	25.98	25.93	25.86	26.29	26.22
CaO	0.5344	0.3963	0.4088	0.4859	0.4173	0.384	0.3985	0.4087	0.4198	0.6491
Na2O	0.0008	0	0.0147	0.0076	0.0001	0.0001	0.0141	0.0083	0.0122	0.0155
Sum	96.65	100.65	99.18	99.45	99.32	99.59	100.18	99.73	99.55	99.41
	Cations per 6 oxygen atoms									
Si	1.945	1.911	1.941	1.933	1.932	1.928804	1.924	1.943	1.918	1.928
Ti	0.001	0.001	0.001	0.000	0.001	0.000525	0.001	0.001	0.000	0.001
Al	0.118	0.134	0.103	0.124	0.122	0.126504	0.131	0.120	0.134	0.124
Cr	0.004	0.005	0.005	0.005	0.006	0.005601	0.006	0.006	0.007	0.006
Fe	0.521	0.496	0.497	0.499	0.504	0.506943	0.515	0.497	0.498	0.488
Mn	0.013	0.012	0.013	0.012	0.013	0.012056	0.013	0.012	0.012	0.012
Mg	1.369	1.444	1.429	1.410	1.410	1.40921	1.400	1.397	1.426	1.422
Ca	0.021	0.015	0.016	0.019	0.016	0.01497	0.015	0.016	0.016	0.025
Na	0.000	0.000	0.001	0.001	0.000	7.05E-06	0.001	0.001	0.001	0.001
Sum	3.993	4.018	4.005	4.002	4.004	4.005	4.007	3.993	4.012	4.007
Mg#	72.4	74.4	74.2	73.9	73.7	73.5	73.1	73.7	74.1	74.5

The upper part of the table shows weight percent oxides of orthopyroxene and clinopyroxene from the SQ-16 sample. The numbers 1 to 4 relate to the regions where the measurement was taken in the sample, c stands for core measurement, b stands for boundary measurements and e stands for exsolution. The lower part of the table shows the number of cations per 6 oxygen atoms. Mg# is defined as the molecular weight percentage Mg/(Mg+Fe).

	Clinopyroxene						
wt%	1 c	1 b	2 c	2 b	3 c	3 b	4 c
SiO2	49.92	49.18	51.78	51.84	52.25	51.96	52.19
TiO2	0.2232	0.2133	0.2021	0.1965	0.1708	0.2284	0.1397
Al2O3	6.3	7.19	3.45	3.38	2.69	3.35	2.98
Cr2O3	0.3645	0.5087	0.3134	0.3251	0.2488	0.3204	0.3438
FeO	6.49	7.17	5.35	5.28	5.25	5.31	5.11
MnO	0.1558	0.1909	0.1714	0.1742	0.1562	0.1817	0.1616
MgO	14.95	14.53	14.93	14.98	15.4	14.87	15.15
CaO	21.1	20.74	23.53	23.93	23.62	23.85	23.82
Na2O	0.3491	0.3272	0.1824	0.1722	0.1515	0.1497	0.1823
Sum	99.85	100.05	99.91	100.28	99.94	100.22	100.0774
	Cations per 6 oxygen atoms						
Si	1.843	1.818	1.910724	1.908	1.926	1.912332	1.922
Ti	0.006	0.006	0.005608	0.005	0.005	0.006321	0.004
Al	0.274	0.313	0.150041	0.147	0.117	0.145309	0.129
Cr	0.011	0.015	0.009143	0.009	0.007	0.009323	0.010
Fe	0.200	0.222	0.165099	0.162	0.162	0.163434	0.157
Mn	0.005	0.006	0.005357	0.005	0.005	0.005664	0.005
Mg	0.823	0.801	0.8213	0.822	0.846	0.815852	0.832
Ca	0.835	0.821	0.930279	0.944	0.933	0.940455	0.940
Na	0.025	0.023	0.01305	0.012	0.011	0.010682	0.013
Sum	4.021	4.024	4.011	4.015	4.012	4.009	4.011
Mg#	80.3	78.3	83.3	83.5	83.9	83.3	84.1

Grain size analysis

Photomicrographs were taken from areas that have clusters or aggregates of either plagioclase or clinopyroxene to avoid measurements of grains that have been limited in their growth by second phase pinning. A number of deformed samples have clinopyroxene and plagioclase grains distributed quite evenly among each other, which posed restrictions in our measurements and resulted in a low amount of measured grains for both plagioclase and clinopyroxene.
The grain size distribution in each sample is plotted in a frequency weighted histrogram of banned grain sizes. Because during grain size measurements there was made no distinction between grains that were dynamically recrystallized or not during the grain size measurements a cut-off value must be determined for each sample. The cut-off value was determined for each sample by looking at the grain size distribution and comparing that with the microstructures. The amount of measured grains and the corrected geometric mean are shown in table 3.

Analysis of the upper mantle xenolith grain sizes

Figure 30 shows the olivine grain size distribution of the mantle xenolith. 345 grain sizes were measured in this sample. The grain size distribution shows a peak between 100-200 μm and the normal distribution likely lies somewhere between 0 and 400 μm. However, the distribution is not uniform as grain sizes up to 800 μm are measured. These grain are correspond to the porphyroclasts in the upper mantle sample which are not dynamically recrystallized. The smallest porphyroclasts are around 450 μm which falls just out of the perceived normal distribution. We therefore take this as the cut off-value. Table 3 show the geometric mean that belongs to the distribution after the cut-off. The geometric mean overlaps with the peak of the distribution.

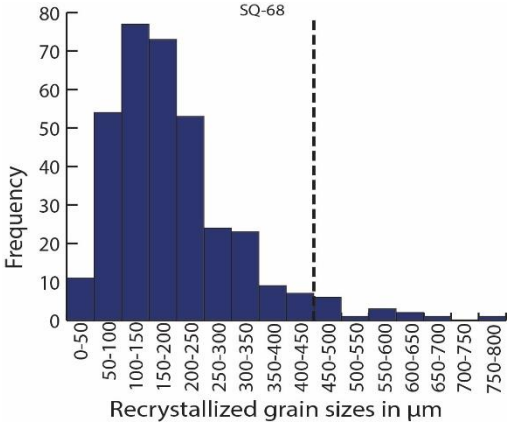

Figure 30: Olivine grain size distribution for the upper mantle xenolith (SQ-68). The cut-off value is shown with the dashed line, all to the right of it is not included in the geometric mean.

Analysis of lower crustal xenolith grain sizes

In the lower crustal xenoliths both plagioclase and clinopyroxene grains have been measured. The grain size distributions of plagioclase is shown in figure 31, and the grain size distributions of clinopyroxene is shown in figure 32. Grain size distributions of SQW-79, SQL-51, SQW-22, SQW-114, SQW-115 and SQW-78 (1) are not shown due to the low number of grains measured. These samples have not been given a cut-off value as the distributions are not likely to be fully representative. The geometric means and differential stresses obtained from these samples are not reliable (table 2). In SQ-16 eight olivine grains have been measured, which are included in table 3.
The plagioclase grain size distribution for SQ-16 shows a clear peak between 100 and 150 μm. However, SQ-16 shows a clear bimodal distribution on the photomicrograph that is not very clear in the distribution. The distribution does show that there are larger grains present in the sample. Many of the larger grains are recrystallized and only the very large grains (<1000 μm) are not considered recrystallized. Therefore the cut-off value for SQ-16 is at 1000 μm. The geometric mean has a value that overlaps with the peak of the distribution.
The plagioclase and clinopyroxene distributions for SQW-75 have a uniform distribution. The microstructure of SQW-75 suggests, however, that the xenolith has had some static recrystallization. There is no clear grain size which has been more affected by this so no cut-off value was determined for this sample. But the geometric mean and the differential stress may be overestimated and underestimated respectively. The geometric means for SQW-75 resemble the peak of the distributions.
The plagioclase distributions of SQW-110 and SQL-48 have no clear peak. In addition SQW-110 appears to have a bimodal grain size distribution. Both samples have fully recrystallized plagioclase so

no cut-off value was applied. The geometric mean falls somewhere in the middle of the distributions for both samples.

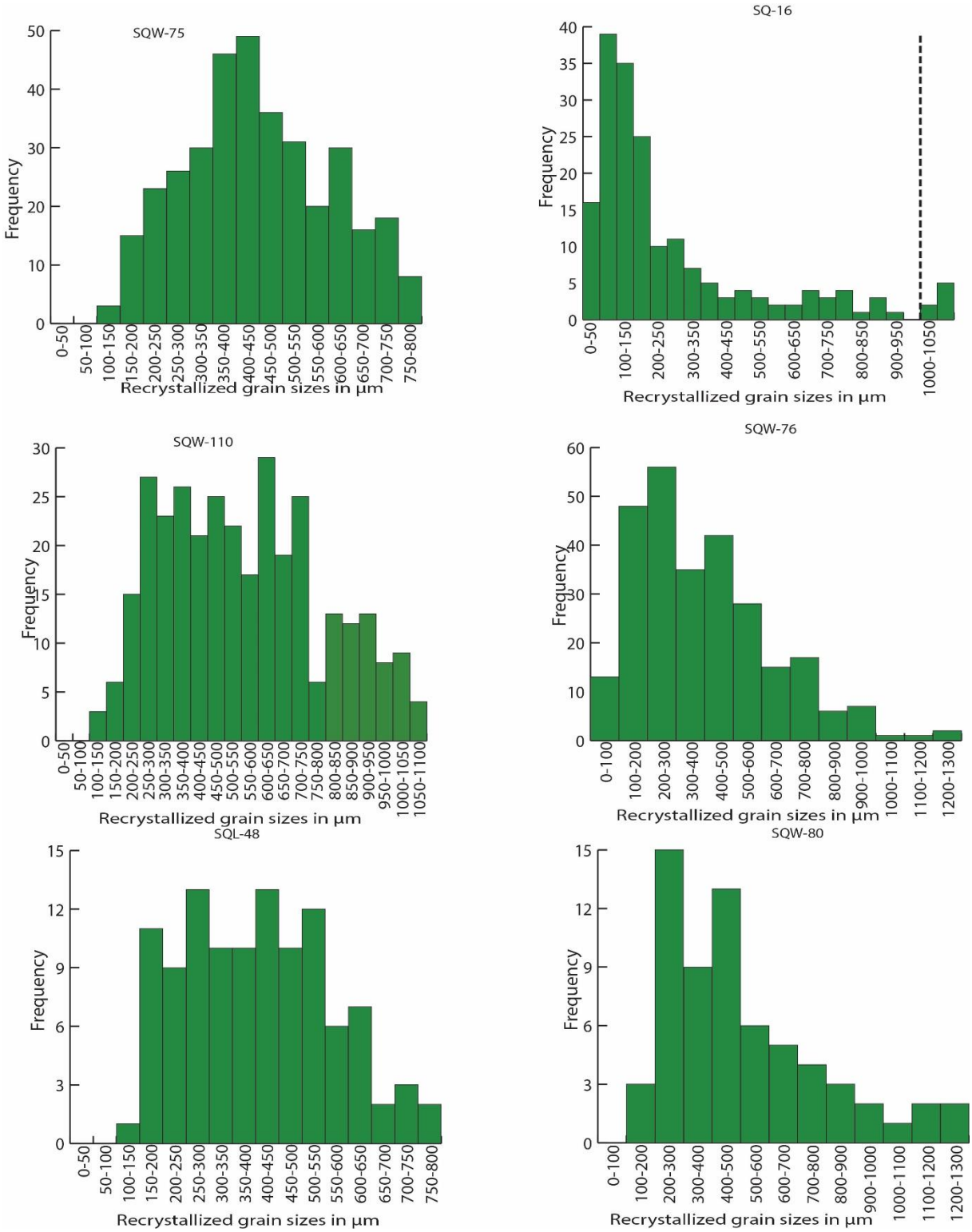

Figure 31: Plagioclase grain size distributions for the lower crustal xenoliths. Most plagioclase are fully recrystallized and only for SQ-16 has a cut-off value.

The clinopyroxene grain size distributions for SQW-80 and SQL-48 are both unimodal. However, both xenoliths contain relic clinopyroxenes with more internal deformation and often smaller cpx surrounding them. For SQW-80 these relic grains are around or larger than 900 µm and for SQL-48 they are around 500 µm or larger. This both seem to fit nicely with the distribution and these values have therefore been used for the cut-off.
The plagioclase distribution of SQW-80 and SQW-76 have a similar asymmetrical shape which may indicate something like static recrystallization of some of the grains, but there is no evidence for that when looking at their microstructures. Plagioclase in both samples are fully recrystallized so no cut-off value was used.

Table 3: Grain size analysis of the deformed lower crustal xenoliths. The geometric means are for recrystallized grains. The non-recrystallized grains are not included.

	Plagioclase		**Clinopyroxene**		**Olivine**	
Sample	No. grains	Geometric mean (µm)	No. Grains	Geometric mean (µm)	No. Grains	Geometric mean (µm)
SQ-68	x	x	x	x	345	158.7
SQ-16	243	126.1	x	x	8	390
SQW-75	391	453.2	298	250.1	x	x
SQW-79	26	667.3	24	467.9	x	x
SQL-48	124	437.2	146	291.3	x	x
SQL-51	39	249	34	403.7	x	x
SQW-78(1)	51	627.1	39	389.9	x	x
SQW-76	272	346.7	x	x	x	x
SQW-110	359	556.3	38	417.7	x	x
SQW-80	63	452.9	99	459.5	x	x
SQW-115	68	548	35	497.9	x	x
SQW-114	x	x	45	368.4	x	x
SQW-22	x	x	37	582.3	x	x

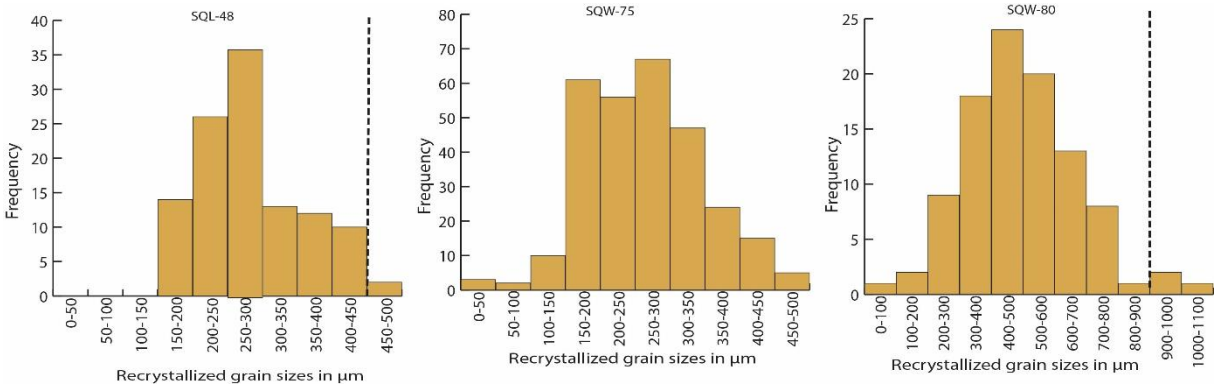

Figure 32: Clinopyroxene grain size distributions for three lower crustal xenoliths. SQL-48 and SQW-80 both have a cut-off value that corresponds to relic clinopyroxene grain sizes.

Paleopiezometry

Table 3 shows the calculated differential stresses for the different phases using the piezometric relations. The stress estimates in the lower crust are on average 10-15 MPa with an outlier of 31.88 MPa when using the Twiss [1977] piezometer for plagioclase and the Mercier [1985] piezometer for clinopyroxene. The piezometer from Post and Tullis [1999] has values that are much too low to be realistic especially when you consider the theoretical piezometer by Twiss as a lower bound. The stresses for plagioclase and clinopyroxene are very similar and differ at most 8 MPa. In addition stress measured with the eight olivines in SQ-16 is comparable with the plagioclase and clinopyroxene estimates.
The stress in the upper mantle seems to be around 30 MPa, which is similar to the stresses obtained for the lower crust and almost identical to the stress obtained for SQ-16.

Table 3: Stress estimates using piezometric relations between recrystallized grain size and stress.

	Upper mantle			
Samples	Olivine	Plagioclase	Post & Tullis [1999]	Clinopyroxene
	Stress in MPa			
SQ-16	29.45	x	x	x
	Lower crust			
	Stress in MPa			
SQ-16	15.55	31.88	0.28	x
SQW-75	x	13.36	0.04	20.6
SQW-79	x	10.27	0.023	10.27
SQL-48	x	13.69	0.043	16.8
SQL-51	x	20.07	0.10	12.09
SQW-78(1)	x	10.71	0.025	12.57
SQW-76	x	16.03	0.061	x
SQW-110	x	11.62	0.030	11.65
SQW-80	x	13.36	0.041	9.99
SQW-115	x	11.74	0.031	9.58
SQW-114	x	x	x	13.39
SQW-22	x	x	x	8.1

For olivine stress estimates the paleopiezometer of van der Wal (1993) is used, for plagioclase Twiss (1977) and for clinopyroxene Mercier (1985)

Water content

The IR measurements have been done on samples SQW-76, SQW- 115 and SQW-78. These samples were chosen as they were also used for the grain size measurement and the xenolith was still big enough to get a thick section out of it. Water peaks are expected at wavelengths between 3000 and 3800 cm^{-1} for both plagioclase and clinopyroxene. The samples were too thick to for the infrared light to completely pass through, which caused the IR spectra to show very high absorbance peaks in the lower wavelength regions. The water measurements do appear fine however.
The IR spectra for plagioclase and clinopyroxene of SQW-115 are shown in figure 33A. There is no water peak in plagioclase and pyroxene spectra that suggest any presence of water.
Figure 33B shows the IR spectra for plagioclase and pyroxene of sample SQW-78. Two plagioclase IR measurements have been taken on this sample and four clinopyroxene IR measurements. Only a very small broad peak is found at a wavelength of 3400 cm^{-1} but peak is too small to be of significance. Clinopyroxene measurements show a broad peak between ~3200 and 3400 cm^{-1}. The area below this

peak has an average of 90 cm^{-1}. Using the beer-lambert law with a pyroxene density of 3.29 g cm^{-3} results in ~770 ppm H_2O.
Figure 33C shows large broad water peak for plagioclase. One IR spectra for plagioclase has no water peak but that is an oddity as three other IR spectra all show large broad water peaks. The smallest area below the water peaks is 208 cm^{-1} which results in ~800 ppm H_2O if a density of 2.65 g cm^{-3} is used for plagioclase.

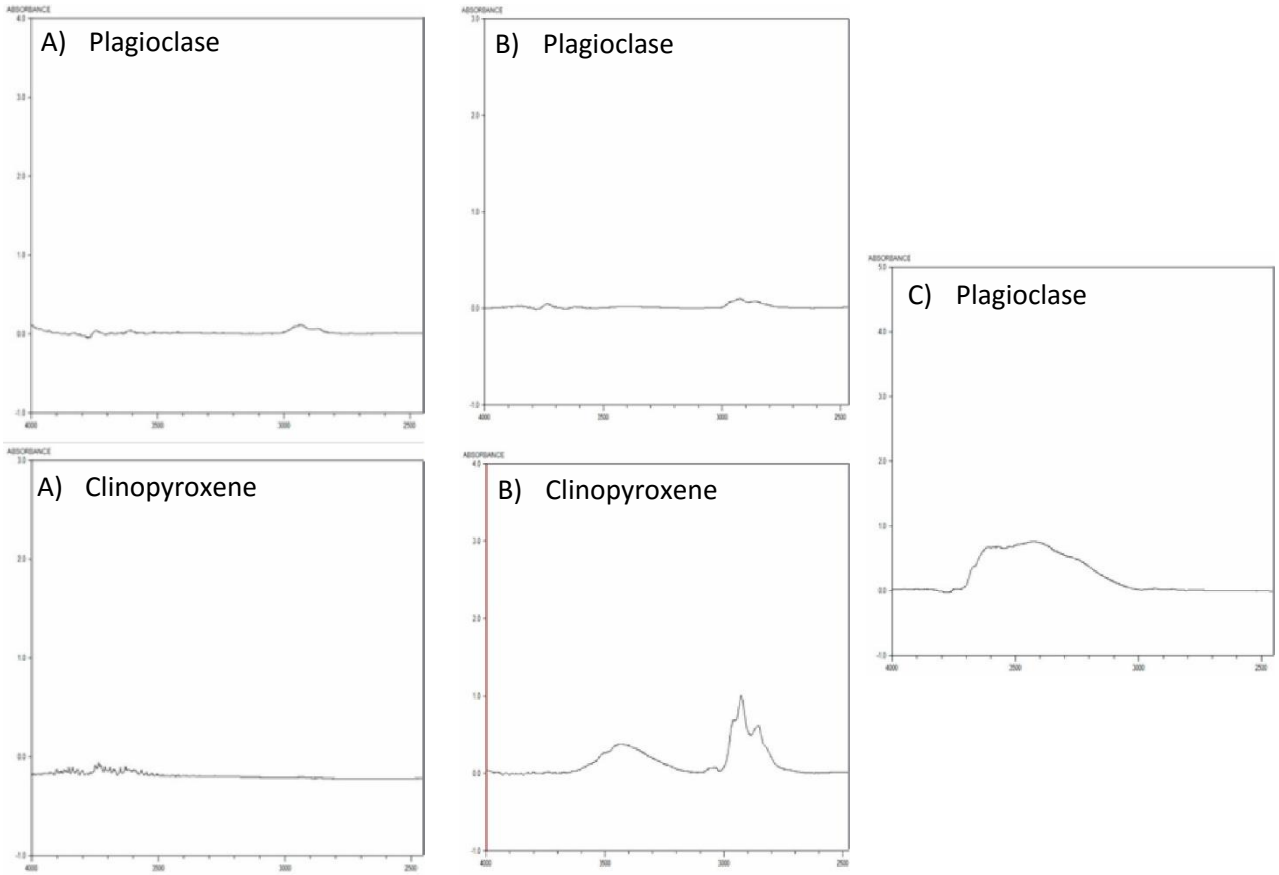

Figure 33: FTIR spectra for lower crustal xenoliths. The spectra are shown for wavelengths range 2500 – 4000 cm^{-1}. A) IR spectra for SQW-115. Both plagioclase and clinopyroxene show no water peaks. B) IR spectra for SQW-78. Plagioclase is almost completely dry but clinopyroxene does have a water peak. C) IR spectrum of plagioclase of xenolith SQW-76. There significant water present in this xenolith.

Discussion

Microstructures

Olivine in the mantle xenolith underwent ductile deformation and dynamic recrystallization as shown from the microstructures. Their bimodal grain size distribution and the undulose extinction of porhyroclasts suggest dynamic recrystallization.
The microstructures of the deformed lower crustal xenoliths are generally consistent among the xenoliths. Clinopyroxene and plagioclase in the lower crustal xenoliths are recrystallized and have irregular grain shapes with interlobate boundaries. These last two microstructural features suggest that clinopyroxene and plagioclase were recrystallized by grain boundary migration, which predominates at high temperatures [Passchier & Trouw, 1996]. The microstructures in the deformed lower crustal xenoliths compare very well with those found by Rosenberg and Stünitz [2003] for high strain and temperature. The presence of triple junctions with 120° degree angles in SQW-75 is characteristic of static recrystallization. However, the only limited presence of triple junctions in the rest xenoliths and the well-preserved irregular grain shapes and interlobate boundaries imply that the dynamically recrystallized grain sizes may have been largely preserved. The preserved dynamically recrystallized grain sizes suggest that the recorded deformation is relative "fresh" as the high temperature in the lower crust would have caused annealing rather fast. Annealing or static recrystallization would have created a foam microstructure, which is not observed in any of the deformed lower crustal xenoliths outside of SQW-75 [Passchier & Trouw, 1996; Rosenberg & Stünitz, 2003]. The recrystallized grain sizes of the lower crustal samples are varied but show a normal distribution. Only the plagioclase grain sizes of xenoliths SQ-16 and SQW-110 show a bimodal distribution. All grains in these xenoliths show evidence of dynamic recrystallization, which indicates that there have probably been more than one deformation phase with a different flow stress. This is further supported by the presence of undulose extinction of some plagioclase grains in sample SQW-22. Mechanical twinning, a strong CPO and the large grain sizes in most of the lower crustal xenoliths indicate that dislocation creep is the dominant deformation mechanism.
Most of the non-deformed gabbros have high pyroxene content. It is possible that because pyroxene is stronger than plagioclase their increased pyroxene content protected these rocks from deformation (personal communication with Martyn Drury). However, it is possible that these are samples that are not included in the shear zone. The non-deformed gabbros studied in the present study compare very well to the lower crustal xenoliths that Berh & Hirth [2014] used to constrain the rheology of the lower crust for the Mojave region. They have similar large grain sizes and are gabbros. The only difference is that the xenoliths that Behr and Hirt recorded had amphiboles, which were not found in xenoliths from the present study. It is possible, however, that the amphiboles have been removed from the samples because of the high temperatures in the lower crust [Personal communication with Holger Stünitz].
SEM analysis shows that SQ-16 and SQW-75 have melt structures that predate the basaltic intrusions found in other samples. These melt structures seem to be mostly along the clinopyroxene boundaries and have likely intruded before or during the deformation.

Compositions, temperature and depth

The compositions of the deformed lower crustal xenoliths are quite uniform. Diopside and anorthite are the two most prominent phases that seem to contain a somewhat even ratio with each other. The mineral compositions of the samples seem to match the description of the Western Baja California Peninsular Range quite well [Gastil, 1975; Kimbrough et al. 2001]. But one deformed sample (SQW-76) has a far more felsic composition than the other samples. This xenolith is likely to have been extracted from a shallower depth than the other lower crustal xenoliths.
The composition of the lower crustal xenoliths falls into the granulite facies which generally corresponds to temperatures above 700 °C. The measured temperature from geothermometry of xenolith SQ-16 ranges 664 – 776 °C, which fits nicely. The melt structures observed in SQ-16 and SQW-75 could indicate that the lower crust was close to melting temperature. But the timing of their intrusion is

unknown. However, according to Rosenberg and Stünitz [2003] grain boundary migration under high temperature and strain is often accompanied by melting, so it is likely that the melt intrusions indicate that the lower crust was near or at melting temperature.
For the upper mantle xenolith temperatures have been reported of 800-950 °C with an equilibrium pressure of <1 GPa. This data can be used to verify geotherms for the Baja California. Figure 34 shows the geotherm of Negrete-Aranda et al., [2013] for the South-central Baja California based on a physical model and the geotherm of Titus et al. [2007] for the San Andreas Fault zone. The data for the upper mantle has a good fit with the geotherm of Titus et al. [2007], which suggests that the Northern Baja California has a similar thermal gradient as that of the San Andreas Fault zone. The thermal gradient for the crust is the same for both geotherms. The lower crustal temperatures seem to correspond to a depth of around 26 – 30 km, which is close to the moho. So both the upper mantle xenolith as the lower crustal xenoliths seem to be derived from sources close to the moho.

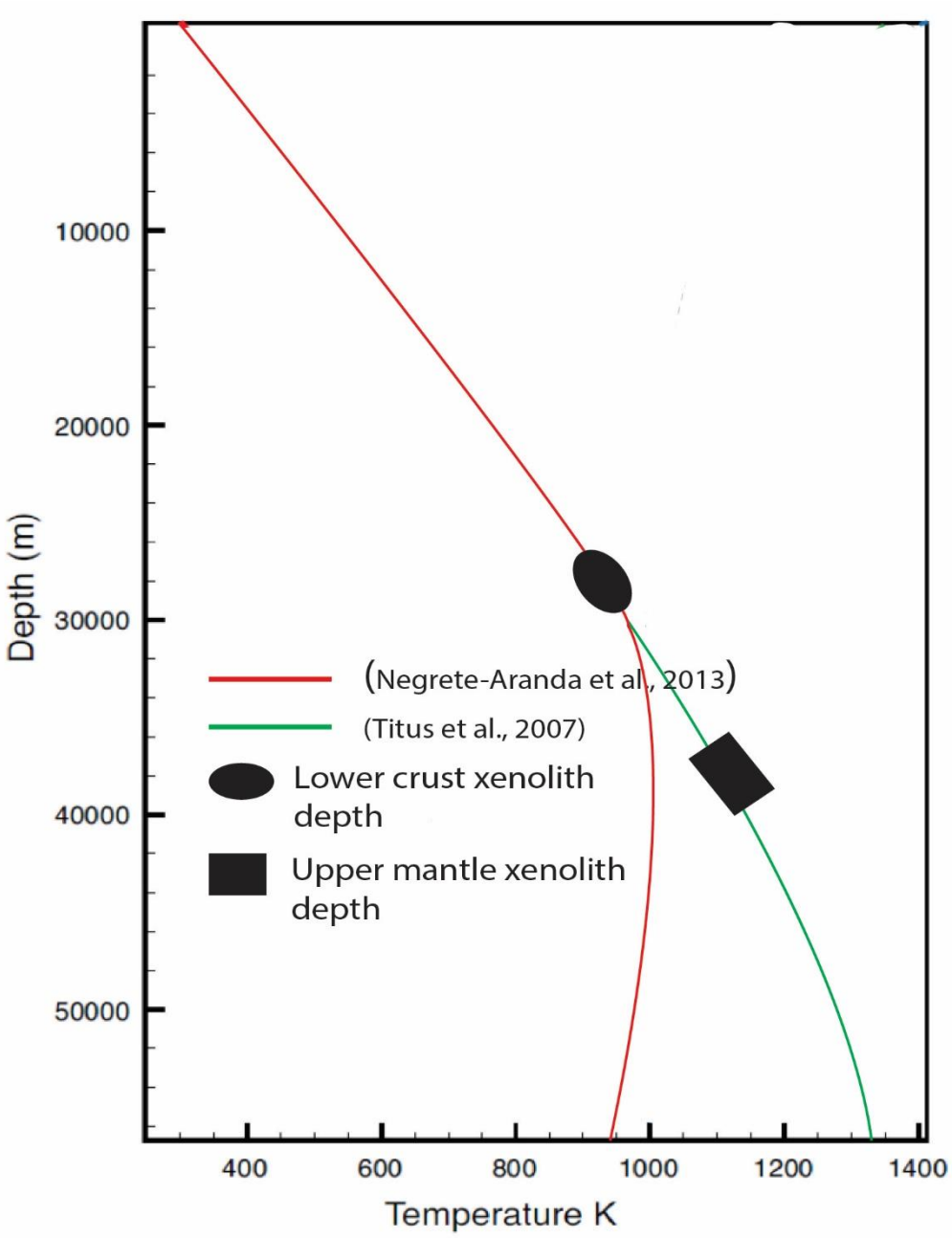

Figure 34: Geotherms for the Baja California and San Andreas Fault zone. The red line shows the geotherm for south-central Baja California. The green line show the geotherm for the San Andreas Fault system. The xenoliths have been plotted on the correct geotherm. After [Negrete-Aranda et al., 2013].

Water content

The mantle xenolith is from the same volcanic region as the mantle xenoliths researched by Palasse et al. (2012). Their samples have almost no water content. It is therefore assumed that our mantle xenolith also contains very little water.
The FTIR measurements of the lower crustal xenoliths show that SQW-115 is completely dry and SQW-76 is predominantly wet. SQW-79 on the other hand has water in clinopyroxene, but not in plagioclase. Experimental data shows that the diffusion of hydrogen in clinopyroxene is faster than that in plagioclase [Johnson, 2003]. Melt structures seem to have accumulated around clinopyroxene in some of the samples (e.g. SQW-75), which may have induced the difference in water content; melt may have brought in more hydrous material. Because the plagioclase is mostly dry in xenolith SQW-75, it is assumed that the whole sample was dry during deformation. IR spectra of SQW-76 show that this xenolith was likely wet during deformation. However, the composition of this sample is much more felsic than the other lower crustal samples, which suggest that it comes from a shallower layer. We assume that SQW-115 and SQW-79 represent the lower crust better than SQW-76 and that the lower crust was therefore dry during deformation.

Reliability of the paleopiezometers

It is generally accepted that the dynamically recrystallized grain size is directly related to the flow stress. The theory behind this however has been debated ever since this relation has been known to exist.
The theoretical piezometer of Twiss (1977) has been heavily criticized in the past. During dynamic recrystallization grains are repeatedly formed and removed thus making it a non-equilibrium dynamic process. However the theoretical piezometer of Twiss applies equilibrium thermodynamics on this process. Therefore the predicted stable grain size by Twiss is the smallest possible but it does not take into consideration that the system can also lower its energy by letting the grain grow [de Bresser et al., 2001]. This means that the differential stress is likely to be underestimated with this theoretical piezometer. Experimental piezometers are generally a better approach as they test the relationship of stress and grain size directly for a set of conditions. The only experimental piezometer available for plagioclase is that of Post and Tullis (1999). The problem with this piezometer is that the conditions used for the deformation experiments are too low for the lower crust. Extrapolating this experimental relationship between recrystallized grain size and stress to the conditions in the lower crust result in differential stresses that are two orders lower than those acquired by the Twiss piezometer. In contrast the experimental clinopyroxene piezometer of Mercier (1985) was made using conditions that are more appropriate for the lower crust. The results of this piezometer very similar to the results gained from the Twiss piezometer. It is therefore assumed that for this research the use of the Twiss piezometer for recrystallized grains of plagioclase is correct.
The experimental piezometer of van der Wal (1993) for olivine in the mantle has been proven to hold true for dry samples and is independent of temperature and pressure [Drury, 2005]. Water contents above ~800 H/Si do have an influence on this piezometric relation [Jung & Karato, 2001] but the San Quintin mantle xenoliths contain very little water [Palasse et al., 2012] so the van der Wal piezometer for olivine is expected to be accurate.

Rheological properties of the upper mantle and the lower crust

The rheological properties of the upper mantle have already been determined by Palasse et al. [2012]. Flow stress in the upper mantle is 10-40 MPa, strain rate ranges $1.1 \times 10^{-14} – 5.7 \times 10^{-15}$ s^{-1} depending on the shear zone thickness in the upper mantle, and corresponding viscosities of $4.4 \times 10^{19} – 3.5 \times 10^{21}$ Pa s. The flow stress measured in the present study for the upper mantle is 30 MPa, which is in the range of stresses reported by Palasse et al. [2012]. A deformation mechanism map constructed with this flow stress and the temperature and equilibrium pressure acquired from literature is shown in figure 35. The

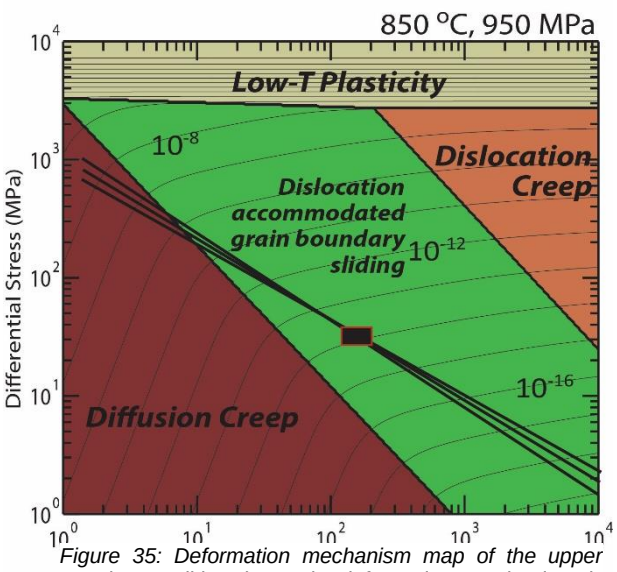

Figure 35: Deformation mechanism map of the upper mantle xenolith. The main deformation mechanism is Dislocation accommodated grain boundary sliding.

corresponding viscosity is ~9.81 x 10^{20} Pa s. Although the dominant deformation mechanism is different than the one Palasse et al. [2012] found, the strain rate and viscosity are still in the same range.

Piezometric results show that the flow stress in the lower crust ranges 10-15 MPa on average and 30 MPa for xenolith SQ-16, which similar as the flow stress in the upper mantle. To determine the lower crustal strain rate the experimental flow law of Dimanov and Dresen [2005] for dry anorthite and diopside, with dislocation creep as the dominant deformation mechanism, has been used. The flow law is of the form:

$$\dot{\varepsilon} = A\sigma^n e^{-Q/RT} \qquad (13)$$

Where $\dot{\varepsilon}$ is the strain rate, A is a material constant (2.71 x 10^{-12} Pa^{-n} s^{-1}), σ is the differential stress (10-30 MPa), Q is the activation energy (723 KJ mol^{-1}), R is the gas constant, and T is the temperature in K (973 K). For the flow law it is assumed that the xenolith contain 50% plagioclase and 50% clinopyroxene. This assumption can be made as the real percentages in the xenoliths are close to that. Strain rate ranges 3.0 x 10^{-14} - 2.64 x 10^{-12} s^{-1} and viscosity ranges 5.68 x 10^{18} – 1.68 x 10^{20} Pa s. In terms of viscosity, the results of the present study suggest that the upper mantle is stronger than the crust by one order of magnitude. In terms of flow stress, however, the two lithospheric layers are of equal strength. These values have been plotted on a deformation mechanism map for dry anorthite (figure 36). If the lower crust was indeed dry during deformation than the xenoliths plot in the dislocation creep.

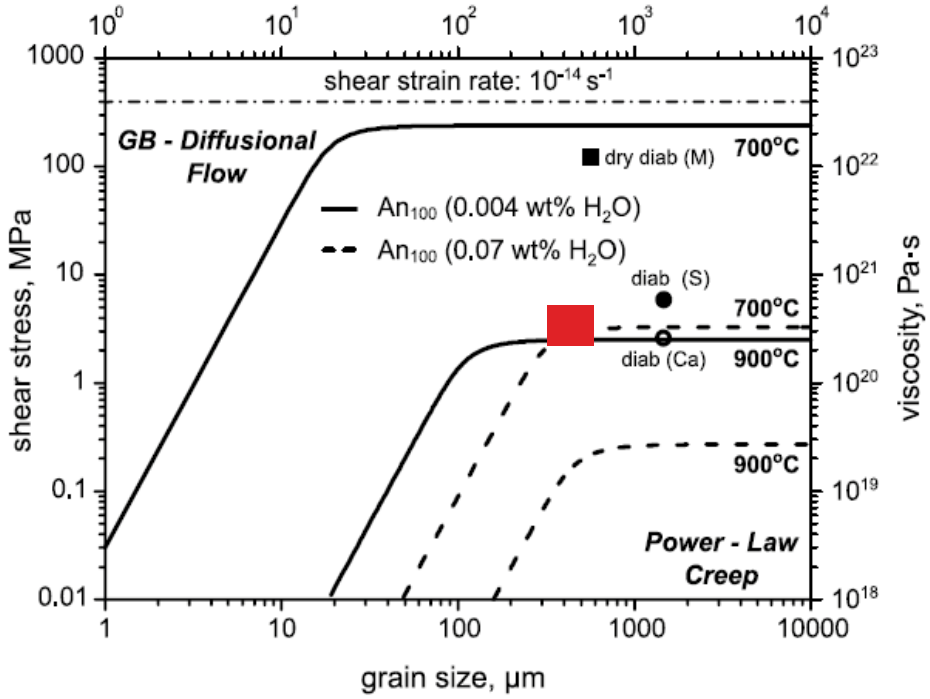

Figure 36: Deformation mechanism map for dry anorthite. The lower crustal range is plotted on the map as a red box based on grain size and shear stress. After [Dresen & Rybacki, 2004].

Based on the estimated differential stress of the upper mantle and the deformed lower crust part of the Baja California strength profile can constrained (figure 37).

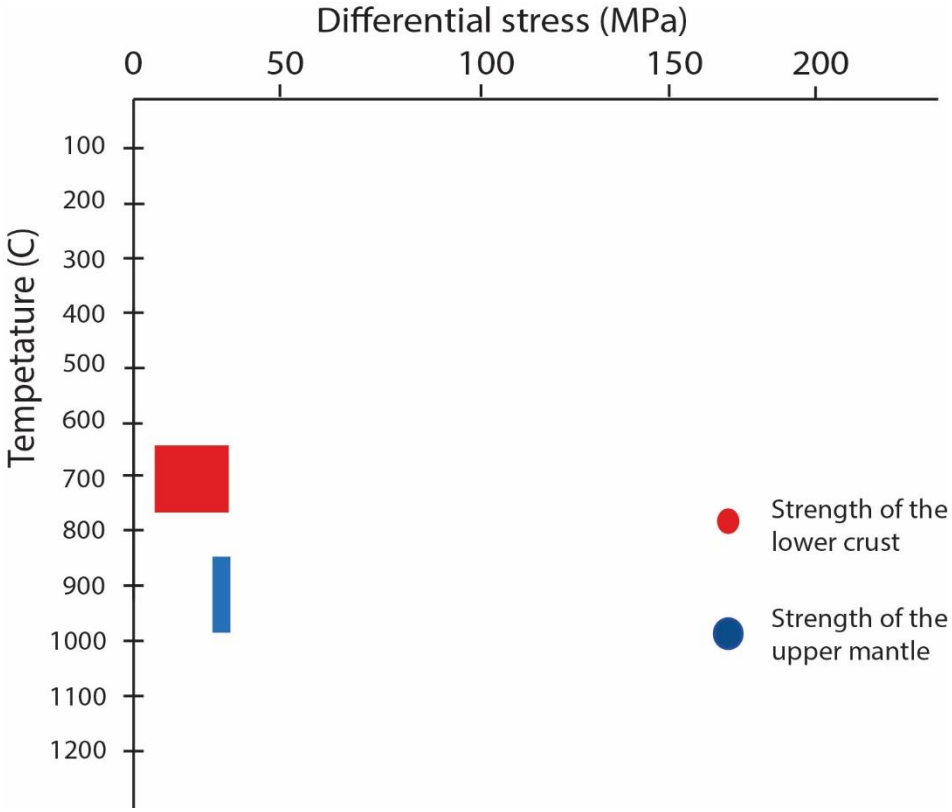

Figure 37: strength of the lower crust and upper mantle plotted against temperature. The strength of the differential stress of the two layers is very similar and might point to a weak upper mantle and lower crust.

Implications and comparison

Our upper mantle rheology is comparable with those of other studies. Chatzaras et al. [2015] estimated upper mantle differential stresses of 10-17 MPa and a viscosity between 7 x 10^{18} and 3.1 x 10^{20} Pa s for the Sand Andreas fault system. Behr and Hirth [2014] found a differential stress of 13-17 MPa for the upper mantle in the Mojave region which corresponds to a mean viscosity of 3 x 10^{19} Pa s. The lower crust is much less constrained in the surrounding area. Behr and Hirth [2014] assumed a strong lower crust based on coarsed grained lower crustal gabbros. Out of these rocks they determined that the lower crust was wet and was subject to dislocation creep and slow strain rates. This is inconsistent with our findings as most of our lower crustal xenoliths are quite strongly deformed. Although a significant amount of our lower crustal xenoliths are non-deformed and are similar to the lower crustal rocks Behr and Hirth [2014] describe which suggests that at least part of the lower crust is strong.
Two tectonic settings are possible: 1) the San Quintin xenoliths sample part of a lithospheric shear zone, which means that the crust and the mantle are both weak and coupled with each other. 2) The crust is moving as a rigid block above a weak ductile upper mantle. In the first case the deformed lower crustal xenoliths are part of the shear zone were as the non-deformed xenoliths were from regions away from the shear zone. In the case of a rigid crust the lower crust may have received part of the ductile deformation of the upper mantle.
The crème brûlée model might fit with the second geological setting, however, the upper mantle xenoliths show no evidence for any strain weakening process which is required for this rheological mode. Furthermore, neither the Jelly sandwich model nor the banana split model fit because the first requires a strong mantle and the second requires strain weakening processes [Burov & Watts, 2006;

Bürgmann & Dresen, 2008]. So none of the general end member rheological models for the continental lithosphere seem to apply to the trans-tensional system of the Baja California.
Recently, a new rheological model for the lithosphere was proposed for strike-slip systems by Chatzaras et al. [2015]. This model is called the lithospheric feedback model and assumes that the viscous mantle deformation and the frictional crustal deformation in fault zones are mechanically coupled but have different tendencies. The mantle spreads the deformation over large areas in the crust whereas the crustal deformation in the form of earthquake rupture tend to localize deformation. These differences cause widespread crustal deformation due to the mantle flow and the crustal deformation causes localized deformation in the mantle [Chatzaras et al., 2015]. Beneath northern Baja California, the dry upper mantle has same order differential stresses and viscosity as the upper mantle beneath the San Andreas fault system reported by Chatzaras et al. [2015]. However, for this model to work the lower crust must kinematically couple the upper crust and the upper mantle which likely includes both rupture and rapid movements during a seismic period and slower movement during an interseismic period. But the lower crustal xenoliths of the Baja California show no sign of rupture and rapid movement. Although such high strain rate structures may not have been brought up by the limited material we have available. A trans-tensional rift system has significant amount of wrench deformation which may cause the system to behave similar to a strike-slip fault zone. So the lithospheric feedback model is plausible in the case of a lithospheric shear zone. However, to be more certain about the rheological properties below Baja California more research must be conducted. Namely on the temperature and depth of the lower crustal xenoliths. The role of the upper crust has also not been constrained in the region.

Conclusions

Olivine recrystallized grain size in the studied mantle xenolith relate reveals a low differential stress of 30 MPa. This fits well with previous results from the mantle xenoliths from the same source which gives upper mantle strain rates of $1.1 \times 10^{-14} – 5.7 \times 10^{-15}$ s^{-1} and viscosities of $4.4 \times 10^{19} – 3.5 \times 10^{21}$ Pa s and a low water content. The gabbroic lower crust also has low water content as well as low differential stresses of ~10-15 MPa. Microstructures suggest that dislocation creep is the main deformation mechanism in the lower crust and dislocation accommodated grain boundary sliding is the main deformation mechanism in the upper mantle. Temperature for one of the Applying an appropriate flow law for the gabbroic lower crust results in a strain rate range of $3.0 \times 10^{-14} - 2.64 \times 10^{-12}$ s^{-1} and a viscosity range of of $5.68 \times 10^{18} – 1.68 \times 10^{20}$ Pa s. The rheological properties of the lower crust and upper mantle seem very similar which can be linked to two different tectonic settings: 1) a lithospheric shear zone; 2) the crust is moving as a rigid block on top of a ductile mantle and part of the lower crust. The lithospheric feedback model seem the best rheological fit for our data and this would suggest that the geological setting is a lithospheric shear zone. Further research must be conducted on depth and temperatures of the lower crustal xenoliths to get better insight on how the rheology is distributed in the lower crust.

Acknowledgements

First and foremost I would like to thank Prof. Dr. Martyn Drury and Dr. Vasileios Chatzaras for their continued guidance and support during the research in Utrecht. Brian Hess (UW-Madison) is thanked for the production of high quality thin sections. Peter van Krieken (UU) is thanked for helping with the FTIR measurements. I also thank Tilly Bouten and Serguei Matveev (UU) for their assistance with the EMP and SEM analysis.

References

Atwater, T., & Stock, J. (1998). Pacific-North America plate tectonics of the Neogene southwestern United States: an update. *International Geology Review*, *40*(5), 375-402.

AvéLallemant, H. G. (1978). Experimental deformation of diopside and websterite. *Tectonophysics*, *48*(1-2), 1-27.

Behr, W. M., & Hirth, G. (2014). Rheological properties of the mantle lid beneath the Mojave region in southern California. *Earth and Planetary Science Letters*, *393*, 60-72.

Behr, W. M., & Platt, J. P. (2014). Brittle faults are weak, yet the ductile middle crust is strong: Implications for lithospheric mechanics. *Geophysical Research Letters*, *41*(22), 8067-8075.

Brace, W. F., & Kohlstedt, D. L. (1980). Limits on lithospheric stress imposed by laboratory experiments. *Journal of Geophysical Research: Solid Earth*, *85*(B11), 6248-6252.

De Bresser, J., Ter Heege, J., & Spiers, C. (2001). Grain size reduction by dynamic recrystallization: can it result in major rheological weakening?.*International Journal of Earth Sciences*, *90*(1), 28-45.

Brey, G. P., & Köhler, T. (1990). Geothermobarometry in four-phase lherzolites II. New thermobarometers, and practical assessment of existing thermobarometers. *Journal of Petrology*, *31*(6), 1353-1378.

Bürgmann, R., & Dresen, G. (2008). Rheology of the lower crust and upper mantle: Evidence from rock mechanics, geodesy, and field observations.*Annual Review of Earth and Planetary Sciences*, *36*(1), 531.

Burov, E. B., & Watts, A. B. (2006). The long-term strength of continental lithosphere:" jelly sandwich" or" crème brûlée"?. *GSA today*, *16*(1), 4.

Byerlee, J. (1978). Friction of rocks. *Pure and applied geophysics*, *116*(4-5), 615-626.

Chatzaras, V., Tikoff, B., Newman, J., Withers, A. C., & Drury, M. R. (2015). Mantle strength of the San Andreas fault system and the role of mantle-crust feedbacks. *Geology*, *43*(10), 891-894.

Chen, X., Lin, C., & Shi, L. (2007). Rheology of the lower crust beneath the northern part of North China: Inferences from lower crustal xenoliths from Hannuoba basalts, Hebei Province, China. *Science in China Series D: Earth Sciences*, *50*(8), 1128-1141.

Dimanov, A., & Dresen, G. (2005). Rheology of synthetic anorthite-diopside aggregates: Implications for ductile shear zones. *Journal of Geophysical Research: Solid Earth*, *110*(B7).

Drury, M. R. (2005). Dynamic recrystallization and strain softening of olivine aggregates in the laboratory and the lithosphere. *Geological Society, London, Special Publications*, *243*(1), 143-158.

Drury, M. R., Vissers, R. L., Van der Wal, D., & Strating, E. H. H. (1991). Shear localisation in upper mantle peridotites. *Pure and Applied Geophysics*,*137*(4), 439-460.

Fletcher, J. M., Grove, M., Kimbrough, D., Lovera, O., & Gehrels, G. E. (2007). Ridge-trench interactions and the Neogene tectonic evolution of the Magdalena shelf and southern Gulf of California: Insights from detrital zircon U-Pb ages from the Magdalena fan and adjacent areas. *Geological Society of America Bulletin*, *119*(11-12), 1313-1336.

Gastil, R. G. (1975). Plutonic zones in the Peninsular Ranges of southern California and northern Baja California. *Geology*, *3*(7), 361-363

Goetze, C., & Evans, B. (1979). Stress and temperature in the bending lithosphere as constrained by experimental rock mechanics. *Geophysical Journal International*, *59*(3), 463-478.

Green, H. W., & Borch, R. S. (1989). A new molten salt cell for precision stress measurement at high pressure. *European Journal of Mineralogy*, 213-220.

Gueydan, F., Précigout, J., & Montesi, L. G. (2014). Strain weakening enables continental plate tectonics. *Tectonophysics*, *631*, 189-196.

Hirth, G., & Kohlstedt, D. (2003). Rheology of the upper mantle and the mantle wedge: A view from the experimentalists. *Inside the subduction Factory*, 83-105.

Homburg, J. M., Hirth, G., & Kelemen, P. B. (2010). Investigation of the strength contrast at the Moho: A case study from the Oman Ophiolite.*Geology*, *38*(8), 679-682.

Johnson, E. A. (2003). *Hydrogen in nominally anhydrous crustal minerals*(Doctoral dissertation, California Institute of Technology).

Johnson, E. A., & Rossman, G. R. (2003). The concentration and speciation of hydrogen in feldspars using FTIR and 1H MAS NMR spectroscopy.*American Mineralogist*, *88*(5-6), 901-911.

Jung, H., & Karato, S. I. (2001). Effects of water on dynamically recrystallized grain-size of olivine. *Journal of Structural Geology*, *23*(9), 1337-1344.

Karato, S. I., Toriumi, M., & Fujii, T. (1980). Dynamic recrystallization of olivine single crystals during high-temperature creep. *Geophysical Research Letters*, *7*(9), 649-652.

Kimbrough, D. L., Smith, D. P., Mahoney, J. B., Moore, T. E., Grove, M., Gastil, R. G., ... & Fanning, C. M. (2001). Forearc-basin sedimentary response to rapid Late Cretaceous batholith emplacement in the Peninsular Ranges of southern and Baja California. *Geology*, *29*(6), 491-494.

Langenheim, V. E., & Jachens, R. C. (2003). Crustal structure of the Peninsular Ranges batholith from magnetic data: Implications for Gulf of California rifting. *Geophysical Research Letters*, *30*(11).

Lopez-Sanchez, M. A., & Llana-Fúnez, S. (2015). An evaluation of different measures of dynamically recrystallized grain size for paleopiezometry or paleowattometry studies. *Solid Earth*, *6*(2), 475.

Mercier J C C. (1985). Olivine and pyroxene. In: Wenk H R, ed. Preferred orientation of metals and Rocks: An Introduction to Modern Texture analysis. *New York: Academic Press Inc. 407—430*

Michaud, F., Royer, J. Y., Bourgois, J., Dyment, J., Calmus, T., Bandy, W., ... & Pontoise, B. (2006). Oceanic-ridge subduction vs. slab break off: Plate tectonic evolution along the Baja California Sur continental margin since 15 Ma. *Geology*, *34*(1), 13-16.

Michibayashi, K. (1993). Syntectonic development of a strain-independent steady-state grain size during mylonitization. *Tectonophysics*, *222*(2), 151-164.

Michibayashi, K., Harigane, Y., Ohara, Y., Muto, J., & Okamoto, A. (2014). Rheological properties of the detachment shear zone of an oceanic core complex inferred by plagioclase flow law: Godzilla Megamullion, Parece Vela back-arc basin, Philippine Sea. *Earth and Planetary Science Letters*, *408*, 16-23.

Mehl, L., & Hirth, G. (2008). Plagioclase preferred orientation in layered mylonites: Evaluation of flow laws for the lower crust. *Journal of Geophysical Research: Solid Earth*, *113*(B5).

Molnar, P. (1992). Brace-Goetze strength profiles, the partitioning of strike-slip and thrust faulting at zones of oblique convergence, and the stress-heat flow paradox of the San Andreas fault. *International Geophysics*, *51*, 435-459.

Nagy, E. A., & Stock, J. M. (2000). Structural controls on the continent-ocean transition in the northern Gulf of California. *Journal of Geophysical Research: Solid Earth*, *105*(B7), 16251-16269.

Negrete-Aranda, R., Contreras, J., & Spelz, R. M. (2013). Viscous dissipation, slab melting, and post-subduction volcanism in south-central Baja California, Mexico. *Geosphere*, *9*(6), 1714-1728.

Olgaard, D. L. (1990). The role of second phase in localizing deformation.*Geological Society, London, Special Publications*, *54*(1), 175-181.

Palasse, L. N., Vissers, R. L. M., Paulssen, H., Basu, A. R., & Drury, M. R. (2012). Microstructural and seismic properties of the upper mantle underneath a rifted continental terrane (Baja California): An example of sub-crustal mechanical asthenosphere?. *Earth and Planetary Science Letters*,*345*, 60-71.

Passchier, C. W., & Trouw, R. A. (1996). *Microtectonics* (Vol. 2). Berlin: Springer.

Paterson, M.S., (1982). The determination of hydroxyl by infrared absorption in quartz, silicate glasses and similar materials. *Bulletin de Mineralogie, 105(1): 20-29.*

Persaud, P., Pérez-Campos, X., & Clayton, R. W. (2007). Crustal thickness variations in the margins of the Gulf of California from receiver functions.*Geophysical Journal International*, *170*(2), 687-699.

Peslier, A. H., & Luhr, J. F. (2006). Hydrogen loss from olivines in mantle xenoliths from Simcoe (USA) and Mexico: mafic alkalic magma ascent rates and water budget of the sub-continental lithosphere. *Earth and Planetary Science Letters*, *242*(3), 302-319.

Peslier, A. H., Luhr, J. F., & Post, J. (2002). Low water contents in pyroxenes from spinel-peridotites of the oxidized, sub-arc mantle wedge.*Earth and Planetary Science Letters*, *201*(1), 69-86.

Plattner, C., Malservisi, R., Dixon, T. H., LaFemina, P., Sella, G. F., Fletcher, J., & Suarez-Vidal, F. (2007). New constraints on relative motion between the Pacific Plate and Baja California microplate (Mexico) from GPS measurements. *Geophysical Journal International*, *170*(3), 1373-1380.

Poirier, J. P. (1985). *Creep of crystals: high-temperature deformation processes in metals, ceramics and minerals*. Cambridge University Press.

Post, A., & Tullis, J. (1999). A recrystallized grain size piezometer for experimentally deformed feldspar aggregates. *Tectonophysics*, *303*(1), 159-173.

Rossman, G. R., Bell, D. R., & Ihinger, P. D. (1995). Quantitative analysis of trace OH in garnet and pyroxenes. *American Mineralogist*, *80*(5-6), 465-474.

Rybacki, E., & Dresen, G. (2004). Deformation mechanism maps for feldspar rocks. *Tectonophysics*, *382*(3), 173-187.

Shimizu, I. (2008). Theories and applicability of grain size piezometers: The role of dynamic recrystallization mechanisms. *Journal of Structural Geology*,*30*(7), 899-917.

Stock, J.M., & Hodges (1989). Pre-pliocene extension around the Gulf of California and the transfer of Baja California to the Pacific plate. *Tectonics, Vol. 8, No. 1, p99-115.*

Taylor, W. R. (1998). An experimental test of some geothermometer and geobaro-meter formulations for upper mantle peridotites with application to the ther-mobarometry of fertile lherzolite and garnet websterite. *Neues Jahrbuch für Mineralogie-Abhandlungen*, 381-408.

Thatcher, W., & Pollitz, F. F. (2008). Temporal evolution of continental lithospheric strength in actively deforming regions. *GSA TODAY*, *18*(4/5), 4.

Twiss, R. J. (1977). Theory and applicability of a recrystallized grain size paleopiezometer. In *Stress in the Earth* (pp. 227-244). Birkhäuser Basel.

Vauchez, A., Tommasi, A., & Mainprice, D. (2012). Faults (shear zones) in the Earth's mantle. *Tectonophysics*, *558*, 1-27.

Van der Wal, D., Chopra, P., Drury, M., & Gerald, J. F. (1993). Relationships between dynamically recrystallized grain size and deformation conditions in experimentally deformed olivine rocks. *Geophysical Research Letters*,*20*(14), 1479-1482.

Wang, Y., Forsyth, D. W., & Savage, B. (2009). Convective upwelling in the mantle beneath the Gulf of California. *Nature*, *462*(7272), 499-501.

Witt-Eickschen, G., & Seck, H. A. (1991). Solubility of Ca and Al in orthopyroxene from spinel peridotite: an improved version of an empirical geothermometer. *Contributions to Mineralogy and Petrology*, *106*(4), 431-439.

Wong, I. G., & Chapman, D. S. (1990). Deep intraplate earthquakes in the western United States and their relationship to lithospheric temperatures.*Bulletin of the Seismological Society of America*, *80*(3), 589-599.

Xia, Q. K., Yang, X. Z., Deloule, E., Sheng, Y. M., & Hao, Y. T. (2006). Water in the lower crustal granulite xenoliths from Nushan, eastern China.*Journal of Geophysical Research: Solid Earth*, *111*(B11).

Zhang, X., Paulssen, H., Lebedev, S., & Meier, T. (2007). Surface wave tomography of the Gulf of California. *Geophysical Research Letters*, *34*(15).

Zhang, X., Paulssen, H., Lebedev, S., & Meier, T. (2009). 3D shear velocity structure beneath the Gulf of California from Rayleigh wave dispersion. *Earth and Planetary Science Letters*, *279*(3), 255-262.

Zhang, X., Paulssen, H., (2011). Geodynamics of the Gulf of California from surface wave tomography

Appendix A

Sample Name	Temp thin section # (Brian's form)	Thin section orientation	Possible YZ Thin section	Photos (Scan filename)	Comments
SQL-48	1 (07/22/2015)	XZ plane. Thin section's long edge parallel to lineation		001	
SQW-78	2 (07/22/2015)	XZ plane. Thin section's long edge parallel to lineation		002	
SQW-110	3 (07/22/2015)	Deviated from XZ plane as sample could not be fed into the cutter at the desired orientation. Thin section's long edge parallel to lineation		003	
SQL-51	4 (07/22/2015)	XZ plane. Thin section's long edge parallel to lineation		004	
SQW-79	5 (07/22/2015)	XZ plane, thin section's SHORT edge parallel to lineation		005	
SQW-114	6 (07/22/2015)	XZ plane, thin section's SHORT edge parallel to lineation		006	
SQW-70	7 (07/22/2015)	XZ plane. Thin section's long edge parallel to lineation		007	
SQW-75	8 (07/22/2015)	XZ plane. Thin section's long edge parallel to lineation		008	
SQW-200	9 (07/22/2015)	Random		009	B. Hess to decide which of two pieces to use for thin section
SQW-95	10 (07/22/2015)	Random		010	
SQW-88	11 (07/22/2015)	Random		011	B. Hess to decide which of two pieces to use for thin section
SQW-81	12 (07/22/2015)	Random		012	
SQW-22	1 (08/24/2015)	XZ plane. Thin section's long edge parallel to lineation		013	
SQL-47 (A,B,C)	2 (08/24/2015)	XZ plane. Thin section's long edge parallel to lineation		014	Three billets cut from same slab.
SQL-100	1 (10/13/2015)	XZ plane. Thin section's long edge parallel to lineation		018	
SQL-13	2 (10/13/2015)	XZ plane. Thin section's long edge parallel to lineation		017	
SQL-12A	3 (10/13/2015)	XZ plane. Thin section's long edge parallel to lineation		020	Slab broke into 2 pieces during sawing. Used bigger piece for billet.
SQW-115	4 (10/13/2015)	XZ plane. Thin section's long edge parallel to lineation		015	
SQW-58 (erroneously named SQW; it is SQL-58)	5 (10/13/2015)	XZ plane. Thin section's long edge parallel to lineation		019	
SQW-80	6 (10/13/2015)	XZ plane. Thin section's long edge parallel to lineation		016	Small sample. Not enough surface area to occupy entire thin section.

SQL-17A	7 (10/13/2015)	XZ plane. Thin section's long edge parallel to lineation		021	
SQL-54	8 (10/13/2015)	XZ plane. Thin section's long edge parallel to lineation		022	
SQW-76	9 (10/13/2015)	XZ plane. Thin section's long edge parallel to lineation		024	Sample was highly fractured. Coated with epoxy before slabbing.
SQW-83	10 (10/13/2015)	XZ plane. Thin section's long edge parallel to lineation		023	Sample was highly friable. Coated with epoxy before slabbing.